Characterizing the marine iodine cycle and its relationship to ocean deoxygenation in an Earth System model

Keyi Cheng[1], Andy Ridgwell[2], Dalton S. Hardisty[1]

[1]Department of Earth and Environmental Sciences, Michigan State University, East Lansing, 48823, USA

[2]Department of Earth and Planetary Sciences, University of California Riverside, Riverside, 92521, USA

Correspondence to: Keyi Cheng (chengkey@msu.edu)

Abstract. Iodine abundance in marine carbonates (measured as an elemental ratio with calcium – I/Ca) is of broad interest as a proxy for local/regional ocean redox. This connection arises because the speciation of iodine in seawater – the balance between iodate (IO_3^-) and iodide (I^-) – is sensitive to the prevalence of oxic vs. anoxic conditions. However, although I/Ca ratios are increasingly commonly being measured in ancient carbonate samples, a fully quantitative interpretation of this proxy requires the availability of a mechanistic interpretative framework for the marine iodine cycle that can account for the extent and intensity of ocean deoxygenation in the past. Here we present and evaluate a representation of marine iodine cycling embedded in an Earth system model ('cGENIE') against both modern and paleo observations. In this framework, we account for IO_3^- uptake and release of I^- through the biological pump, the reduction of ambient IO_3^- to I^- in the water column, plus the re-oxidation of I^- to IO_3^-. We develop and test a variety of different plausible mechanisms for iodine reduction and oxidation transformation and contrast model projections against an updated compilation of observed dissolved IO_3^- and I^- concentrations in the present-day ocean.

By optimizing the parameters controlling previously proposed mechanisms involved in marine iodine cycling, we find that we can obtain broad matches to observed iodine speciation gradients in zonal surface distribution, depth profiles, and oxygen deficient zones (ODZs). However, we also identify alternative, equally well performing mechanisms which assume a more explicit mechanistic link between iodine transformation and environment – an ambiguity that highlights the need for more process-based studies on modern marine iodine cycling. Finally, to help distinguish between competing representations of the marine iodine cycle and because our ultimate motivation is to further our ability to reconstruct ocean oxygenation in the geological past, we conducted 'plausibility tests' of different model schemes against available I/Ca measurements made on Cretaceous carbonates – a time of substantially depleted ocean oxygen availability compared to modern and hence a strong test of our model. Overall, the simultaneous broad match we can achieve between modelled iodine speciation and modern observations, and between forward-proxy modelled I/Ca and geological elemental ratios, supports the application of our Earth system modelling in simulating the marine iodine cycle to help interpret and constrain the redox evolution of past oceans.

## 1.	Introduction

Dissolved Iodine (I) in seawater is redox sensitive and as such, is a potential invaluable delineator of past ocean deoxygenation. This arises directly from: (1) observations that the oxidized form of iodine (iodate, IO_3^-) is reduced to iodide (I^-) under low oxygen conditions, and (2) that IO_3^- in seawater is incorporated into carbonate lattice during precipitation in proportion to its seawater abundance (whilst I^- is not) (Lu et al., 2010; Podder et al., 2017; Kerisit et al., 2018; Zhang et al., 2013; Hashim et al., 2022). As a result, past ocean IO_3^- concentrations can be recorded in coeval carbonates as I/Ca ratios, with the potential for carbonate I/Ca to reflect the redox variation of the ancient seawater (Lu et al., 2010). Indeed, the I/Ca ratio in marine carbonates is already being applied widely as a paleoredox proxy, with studies employing it to explore variations in the dissolved oxygen ($[O_2]$) concentration of seawater throughout much of Earth history, from the Archean and through the Cenozoic (Lu et al., 2010; Hardisty et al., 2014; Zhou et al., 2015; Lu et al., 2016; Edwards et al., 2018; Lu et al., 2018; Bowman et al., 2020; Pohl et al., 2021; Wei et al., 2021; Ding et al., 2022; Shang et al., 2019; Liu et al., 2020; Fang et al., 2022; Uahengo et al., 2020; Yu et al., 2022; Tang et al., 2023). However, realizing the full potential for I/Ca to provide critical insights into how the oxygenation of the ocean has evolve through time, as well as the causes and biological/ecological consequences of this, requires that we have an adequate understanding, not only of carbonate IO_3^- incorporation, but of the dynamics of the marine iodine cycle in general.

Considerable progress has been made over the past few decades towards the goal of understanding the marine iodine cycle. Iodine has a relatively long residence time in the ocean (~300 kyr; Broecker and Peng, 1983) leading to its concentration being relatively constant throughout the global ocean (at around 500 nM) (Elderfield and Truesdale, 1980; Truesdale et al., 2000; Chance et al., 2014). However, although the total concentration of dissolved iodine is relatively invariant, the two most abundant species of dissolved iodine in the ocean, IO_3^- and I^-, vary relative to each other depending on the environment. Today, IO_3^- is generally the dominant iodine species in oxygenated regions of the ocean where it represents total iodine nearly quantitatively below the euphotic zone. Within the euphotic zone, the concentration of I^- generally increases in association with release during phytoplankton growth and senescence (Hepach et al., 2020). Within ODZs, IO_3^- is reduced to I^- – but not always quantitatively so – and hence is present only at relatively low concentrations while I^- is abundant (Truesdale et al., 2000; Rue et al., 1997; Cutter et al., 2018; Moriyasu et al., 2020; Farrenkopf and Luther, 2002; Wong and Brewer, 1977; Truesdale et al., 2013; Rapp et al., 2020, 2019).

Although IO_3^- is generally depleted in low-$[O_2]$ settings, the relationship between seawater $[O_2]$ and $[IO_3^-]$ is not simple and is not currently well understood. Recently published observations from ODZs in the ocean reveals that the relationship between dissolved $[O_2]$ and $[IO_3^-]$ is not linear, but instead it is possible that there is a certain $[O_2]$ or related redox threshold associated with triggering IO_3^- reduction (Cutter et al., 2018; Moriyasu et al., 2020; Farrenkopf and Luther, 2002; Rue et al., 1997; Chapman, 1983). Dissimilatory IO_3^- reducing bacteria, as well as abiotic reduction with sulfide and dissolved Fe, have been identified within ODZs (Farrenkopf et al., 1997; Councell et al., 1997; Jiang et al., 2023). In addition, slow oxidation-reduction kinetics (Tsunogai, 1971; Hardisty et al., 2020; Schnur et al., 2024) imply the likelihood that *in situ* iodine signals could be integrated across large-scale physical oceanography processes – including ocean currents and mixing between water masses (Hardisty et al., 2021), and meaning that iodine

2

70 speciation reflects regional rather than strictly *in situ* redox conditions (Lu et al., 2020b). Non-redox related processes,

71 such as phytoplankton-mediated IO_3^- reduction and organic matter remineralization also exert controls on iodine

72 speciation in the water column (Fig. 1; Elderfield and Truesdale, 1980; Wong et al., 1985; Luther and Campbell, 1991;

73 Hepach et al., 2020). Therefore, it is difficult to infer water column redox simply based on iodine speciation without

74 considering these interacting physical and biological effects.

75

76

77
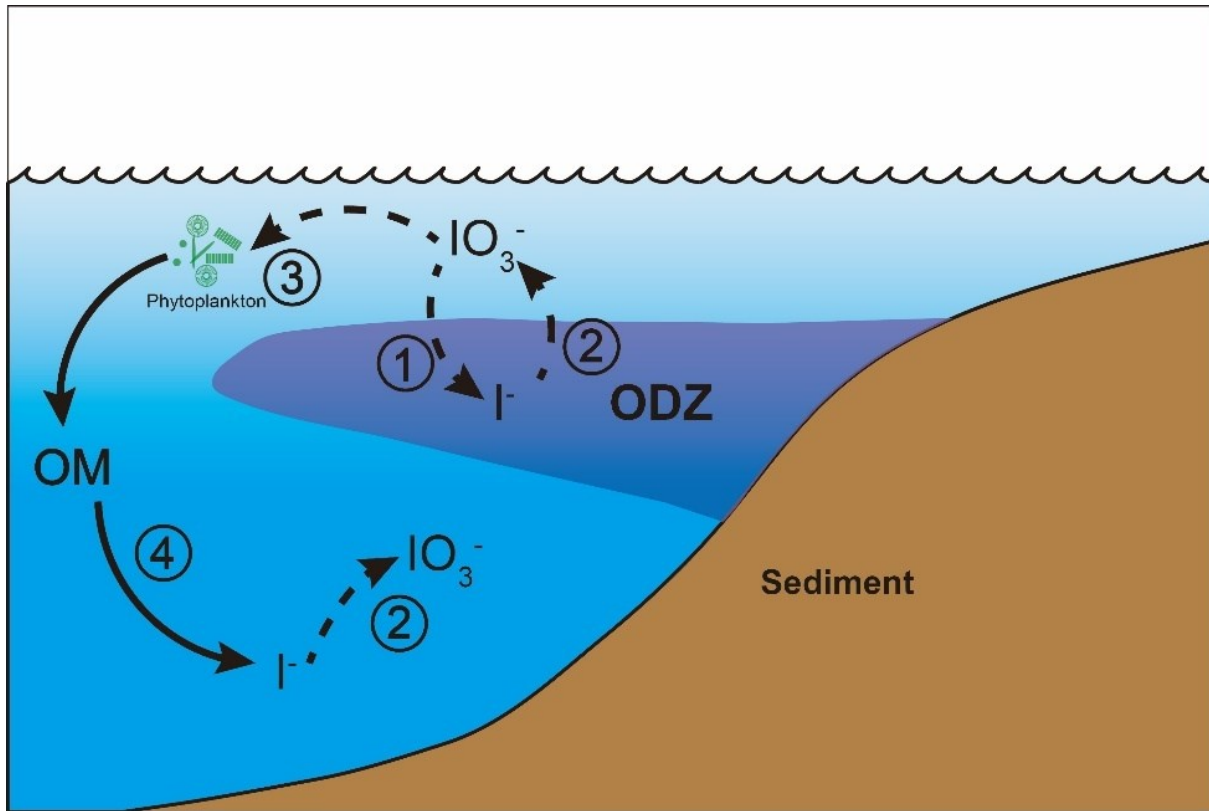
Figure 1: The iodine cycle in marine oxygen deficient zones (ODZ) in cGENIE including (1) IO_3^- reduction to I^-, (2) re-oxidation of I^- to IO_3^-, (3) photosynthetic IO_3^- update by phytoplankton, and (4) I^- releasement from organic matter (OM) through remineralization. The detailed oxidation-reduction options are described in Section 2.2 and Table 1. Dashed arrows indicate variable processes during ensemble simulations.

82

83 Aside from the uncertainties associated with IO_3^- reduction, it is notable that the oxidants responsible for IO_3^-

84 formation during I^- re-oxidation are currently unknown, only that it is unlikely to be free O_2, which is not

85 thermodynamically favorable to oxidize I^- (Luther et al., 1995). A recent thermodynamic review indicates that reactive

86 oxygen species (ROS) such as hydrogen peroxide and OH radicals can fully oxidize I^- to IO_3^-. Iodide oxidation to IO_3^-

87 is a 6-electron transfer and other ROS, such as superoxide, are only thermodynamically favorable to catalyze partial

88 oxidation to intermediates (Luther, 2023). These ROS species have heterogenous distributions and ambient ocean

89 concentrations that are typically relatively low compared to iodine, supporting the likelihood of temporally or spatially

90 isolated high I^- oxidation rates despite of overall extremely slow rates (Schnur et al., 2024). Additional support for

spatially or temporally heterogenous I$^-$ oxidation rates comes from recent experimental observations of IO$_3^-$ production from I$^-$ in nitrifying cultures (Hughes et al., 2021). Nitrification (oxidation of NH$_4^+$ to NO$_2^-$ (and NO$_3^-$)) rates vary globally, with the highest values occurring in ODZs and the deep chlorophyl maximum (summarized in Table 2 of Hughes et al., 2021). Regardless, nitrification or other specific mechanisms have yet to be linked directly to I$^-$ oxidation under normal marine conditions, leaving open the question of rates and locations of I$^-$ oxidation.

Despite a growing understanding of I/Ca variations through geologic time, it remains challenging to determine the mechanisms responsible for controlling the spatiotemporal patterns of marine [IO$_3^-$] and how these are linked to seawater oxygen and there have only been a few attempts to date to model the marine iodine cycle. In a recent publication, a model was developed to simulate modern ocean surface I$^-$ distributions, with the aim of being able to improve tropospheric ozone models (Wadley et al., 2020). This particular model was based around a relatively high horizontal ocean resolution (1° grid size) with a 3-layer vertical upper water column. Iodine biogeochemical cycling was coupled with the nitrogen cycle, with the surface I$^-$ distribution sensitive to biological and hydrological factors including primary productivity, I:C ratio, oxidation, mixed layer depth, advection, and freshwater flux. Because the Wadley et al., (2020) model was specifically focused on near-surface processes within the upper 500 m, it did not consider processes occurring within ODZs and hence is not directly applicable to questions concerning the controls on I/Ca ratios. In contrast, a second model-based study deliberately targeted paleoceanographic questions and incorporated an iodine cycle including redox-controlled biogeochemical reactions into the 'cGENIE' Earth system model (Lu et al., 2018). The advantage for paleo studies afforded by this particular approach is that the cGENIE model can take into account different continental configurations, non-modern atmospheric composition (pO$_2$, pCO$_2$), and other boundary conditions that may have differed on ancient Earth relative to today (Ridgwell et al., 2007; Reinhard et al., 2016; Boscolo-Galazzo et al., 2021; Remmelzwaal et al., 2019; Pohl et al., 2022; Reinhard and Planavsky, 2022).

Here, we calibrate the iodine cycle within the cGENIE Earth System model to provide a mechanistic framework for interpreting ancient I/Ca variations. In this study, we build on the work of Lu et al., (2018) and further develop and test a series of new potential parameterizations for water column iodine oxidation and reduction (in addition to reduction and transport associated with the biological pump). We also developed 3 criteria for assessing the model: (1) Statistical evaluation using the 'model skill score' (M-score) (Watterson, 1996) – a non-dimensional measure calculated using location-dependent comparisons between the model and an iodine ocean observation data compilation. (2) Graphical comparison of modeled and observed iodine across 3 illustrative iodine speciation gradients (depth profiles from multiple ocean basins, latitudinal transects of surface waters, and across transects of the Eastern Tropical North Pacific oxygen minimum zone (Moriyasu et al., 2020)). (3) Model applicability to ancient settings by comparing (also using the M-score) projections of ocean surface I/Ca with published I/Ca data from the Cretaceous (Zhou et al., 2015).

2.   Model Description

2.1   The cGENIE Earth system modelling framework

cGENIE is a class of model known as an 'Earth system model with intermediate complexity' (EMIC) – a global climate-carbon cycle model that simplifies one or more (typically physical climate) components of the Earth system. In the case of cGENIE, ocean circulation is solved for on a relatively low-resolution grid (here: an equal area 36×36 grid, which equates to $10°$ in longitude and latitude increments from $3°$ near the equator to $20°$ near the poles, and with 16 non-equally spaced vertical levels). This is coupled to a 2D energy-moisture-balance-model (EMBM) and a 2D dynamic-thermodynamic sea-ice model. The physics are described in (Marsh et al., 2011; Edwards and Marsh, 2005).

Representation of the primary factors controlling the oceanic iodine cycle – specifically, biological productivity, remineralization, and water column redox – follow Crichton et al., (2021). In this configuration, the rate of organic matter export from the ocean surface is calculated based on just a single nutrient (phosphate) control (together with modifiers reflecting ambient light, sea-ice cover, and temperature) and assumes a Redfield-ratio stoichiometry (1:106) with carbon (Fig. 1). Organic matter is partitioned into particulate (POM) (33% of total export) and dissolved forms (DOM) (67%), with the former sinking down through the water column where it is progressively remineralized at a rate scaling with ambient temperature (described in Crichton et al., 2021 and Boscolo-Galazzo et al., 2021). When dissolved oxygen nears depletion, sulphate (SO_4^{2-}) is assumed to be consumd as an electron acceptor to support the remineralization of organic matter (both POM and DOM). The rate of POM remineralization in the water column is governed only by ambient temperature which, in conjunction with a prescribed sinking rate, deterines the vertical distribution of solute release and oxidant consumption. The relative availablity of dissolved O_2 vs. SO_4^{2-} determines the proportion of organic matter degraded by each electron acceptor. In this, the relative consumption of SO_4^{2-} is goverened by a SO_4^{2-} half-saturation limitation term as well as a dissolved oxygen (O_2) inhibition term, while oxic resperation of organic matter is restricted by an $[O_2]$ half-saturaion limitation term (described in Reinhard et al., 2020). Sulphate can hence be consumed even before dissolved oxygen can become fully depleted. For DOM, a decay constant (here: 0.5 years) determines the total fraction that is remineralized per unit time. It should be noted that currently, there is no published nitrogen cycle in the cGENIE model framework and we do not consider nitrate reduction as part of the redox cascade here.

2.2   Marine iodine cycling in cGENIE

In the cGENIE model, iodine is present in three reservoirs: IO_3^- and I^- in the water column, and I^- incorporated in POM (and DOM). We then consider four processes that transfer iodine between these reservoirs (summarized in Fig. 1): (1) IO_3^- reduction in the water column, (2) I^- oxidation (also in the water column), (3) photosynthetic IO_3^- uptake (and assumed intercellular reduction to I^-), and (4) I^- release to seawater during the remineralization of POM (and DOM). As dissolved species, IO_3^- and I^- are physically transported and mixed through ocean circulation (as is I incorporated into DOM), whereas iodine in POM settles vertically through the water column. This is the same overall framework used by Lu et al., (2018). In this paper we re-assess this framework against an updated compilation of observed iodine

159   speciation in the modern ocean and develop and test alternative representations of IO_3^- reduction (process (1),

160   'threshold', 'inhibition', and 'reminSO4lifetime') and I^- re-oxidation (process (2), 'lifetime', 'Fennel', and

161   'reminO2lifetime'). Although we describe all 5 different parameterizations below for completeness and a number of

162   different permutations of 3 IO_3^- reduction and 3 I^- re-oxidation processes (presented in S.I.), in this paper we will focus

163   primarily on a single reduction parameterization ('threshold') in combination with the 3 different re-oxidation schemes.

164   **2.2.1 IO_3^- reduction schemes**

165   • **'threshold'**. In the numerical scheme of Lu et al., (2018), when $[O_2]$ falls below a set concentration threshold,

166   IO_3^- is immediately and quantitatively reduced to I^- (thereafter, we term this IO_3^- reduction parameterization

167   'threshold').

168   • **'inhibition'**. The 'inhibition' scheme links the IO_3^- reduction rate with the ambient O_2 concentration. Following

169   the formulation for the rate of SO_4^{2-} reduction in Reinhard et al., (2020), we apply an oxygen inhibition term

170   governed by a half-saturation constant. In devising this scheme, we note that while IO_3^- reduction rates have been

171   determined experimentally, the quantitative relationship with $[O_2]$ (or other parameters) is unknown. The IO_3^-

172   reduction under 'inhibition' is mathematically described as:

173       $$d[IO_3^-]/dt = [IO_3^-] \times k_{red} \times \frac{k_{O_2}}{k_{O_2}+[O_2]}$$ (1)

174   in which k_{red} is the maximum first-order reduction rate of IO_3^-, and k_{O2} is the half-saturation constant of O_2.

175   • **'reminSO4lifetime'.** Reduced sulfur (e.g. sulfides) is also suspected to play an important role in IO_3^- reduction

176   in seawater, especially in the sulfidic zones (Jia-zhong and Whitfield, 1986; Luther and Campbell, 1991; Wong

177   and Brewer, 1977; Truesdale et al., 2013). We therefore devise a scheme ('reminSO4lifetime') that scales a

178   nominal 'lifetime' for IO_3^- with the rate of SO_4^{2-} reduction in the model. This has the effect of increasing the rate

179   of IO_3^- reduction (a shorter lifetime) under conditions of higher sulphate reduction rates and hence lower ambient

180   oxygen concentrations and/or higher rates of organic matter degradation:

181       $$d[IO_3^-]/dt = [IO_3^-] \times \frac{1}{\tau_{sul}} \times d[SO_4^{2-}]/dt$$ (2)

182   in which τ_{sul} defines the rate constant parameter linking the IO_3^- and SO_4^{2-} reduction, while the $d[SO_4^{2-}]$ is amount

183   of SO_4^{2-} reduced during each model timestep.

184   **2.2.2 I^- oxidation schemes**

185   • **'lifetime'**. In Lu et al., (2018), I^- is oxidized to IO_3^- following first-order kinetics regardless of ambient O_2 (scheme

186   'lifetime'). In this scheme, I^- oxidation follows the first-order reaction kinetics:

187       $$d[I^-]/dt = [I^-] \times \frac{1}{\tau}$$ (3)

188   where τ is the lifetime of I^- in seawater.

189   • **'Fennel'**. Given the overlapping redox potential between I and N (e.g. Rue et al., 1997; Cutter et al., 2018), we

190   explore the potential for a link between areas of I^- and nitrification. To simulate this, we devise an alternative

191   'Fennel' scheme, in which I^- oxidation rates vary as a function of ambient O_2, increasing with ambient O_2

192   concentrations towards some hypothetical maximum value following Michaelis–Menten kinetics (Fennel et al.,

193   2005). In Fennel et al., (2005), this parameterization was originally devised for ammonia reoxidation. The form

194   of this response is defined by the maximum reaction rate and O_2 half-saturation constant (Fennel et al., 2005):

195 $$d[\text{I}^-]/dt = [\text{I}^-] \times k_{ox} \times \frac{[O_2]}{k_{fenn}+[O_2]} \qquad (4)$$

196   in which k_{ox} defines the maximum rate constant of I$^-$ oxidation, while k_{fenn} is the O$_2$ half-saturation constant.

197 • **'reminO2lifetime'.** Finally, in 'reminO2lifetime', we associate I$^-$ oxidation with O$_2$ consumption during

198   remineralization. The logic behind this parameterization is the recent observation of I$^-$ oxidation to IO$_3^-$ catalyzed

199   by bacteria, perhaps in association with ammonia oxidation (Hughes et al., 2021). Although the nitrogen cycle is

200   not currently included in cGENIE, the NH$_4^+$ oxidation can be scaled to OM remineralization (Martin et al., 2019)

201   and hence to O$_2$ consumption during remineralization. Under 'reminO2lifetime', the lifetime of I$^-$ oxidation is

202   inversely linked to O$_2$ consumption so that faster remineralization – which in the ocean leads to more intensive

203   NH$_4^+$ oxidation – enhances I$^-$ oxidation. This I$^-$ oxidation scheme follow this equation:

204 $$d[\text{I}^-]/dt = [\text{I}^-] \times \frac{1}{\tau_{O2}} \times d[O_2]/dt \qquad (5)$$

205 where τ_{O2} is the rate constant parameter and $d[O_2]$ is the O$_2$ consumption during remineralization during a single

206 timestep in the model.

2.2.3 Biological reduction pump

208 The final pair of coupled processes in the marine iodine cycle framework concerns the processing of iodine directly

209 through the biological pump. Phytoplankton-absorbed iodine is stored in the cell as IO$_3^-$, I$^-$, or other forms, followed

210 by release during senescence (Hepach et al., 2020). While there is some uncertainty as to whether IO$_3^-$ reduction is

211 assimilatory or dissimilatory (Hepach et al., 2020), we adopt a comparable approach to nitrogen cycling (sequence:

212 NO$_3^-$ uptake, N incorporation into organic matter, remineralization and release as the reduced NH$_4^+$ form). We assume

213 that IO$_3^-$ is assimilated by phytoplankton and incorporated into POM during photosynthesis (Elderfield and Truesdale,

214 1980) and released as I$^-$ during remineralization and/or cell senescence (Wong et al., 2002; Hepach et al., 2020; Wong

215 et al., 1985). cGENIE simulates these processes via an assumed 'Redfield-ratio' of iodine to carbon (I:C ratio) in OM.

216 We note that while the value of I:C can be adjusted in the model, it is currently assumed fixed in value throughout the

217 ocean. We discuss the merits of an optimized and uniform I:C compared to variable I:C (e.g., Wadley et al., 2020) in

218 more detail in the Discussion.

2.3 Model-data evaluation

220 For evaluating the marine iodine cycle in the cGENIE model, we compiled oceanic iodine observation data from the

221 literature (Fig. 2; Table S4). Our dataset builds on the compilation of Chance et al., (2019), which was used to calibrate

222 the Wadley et al., (2020) model, but includes more recent publications (referenced in Table S4) and is also expanded

223 to include the deep ocean and ODZ data. To avoid the influence of freshwater dilution and recycled iodine from the

224 sedimentary flux, we applied a filter which only keeps the measurements with total iodine (or IO$_3^-$ plus I$^-$) between

225 450 nM and 550 nM in the dataset. Note that the I$^-$ measurements from the GP16 cruise in the ETSP are not included

226 for the comparison because of potential method considerations (see Cutter et al., 2018 and Moriyasu et al., 2023).

227 After filtering, the data were gridded to the cGENIE model grid (provided as .nc files in Supplementary Material).

228   We used the model skill measure (M-score) (Watterson, 1996) to assess the performance of the marine iodine

229 cycle in cGENIE compared to the gridded data. For each iodine speciation (hereby IO$_3^-$ and I$^-$), a M-score value is

calculated through comparing gridded observations versus model results in each corresponding grid (Fig. 2). The synthesized M-score for iodine of each model experiment is calculated through averaging those for both I$^-$ and IO$_3^-$. The higher the M-score value the better the model-data performance.
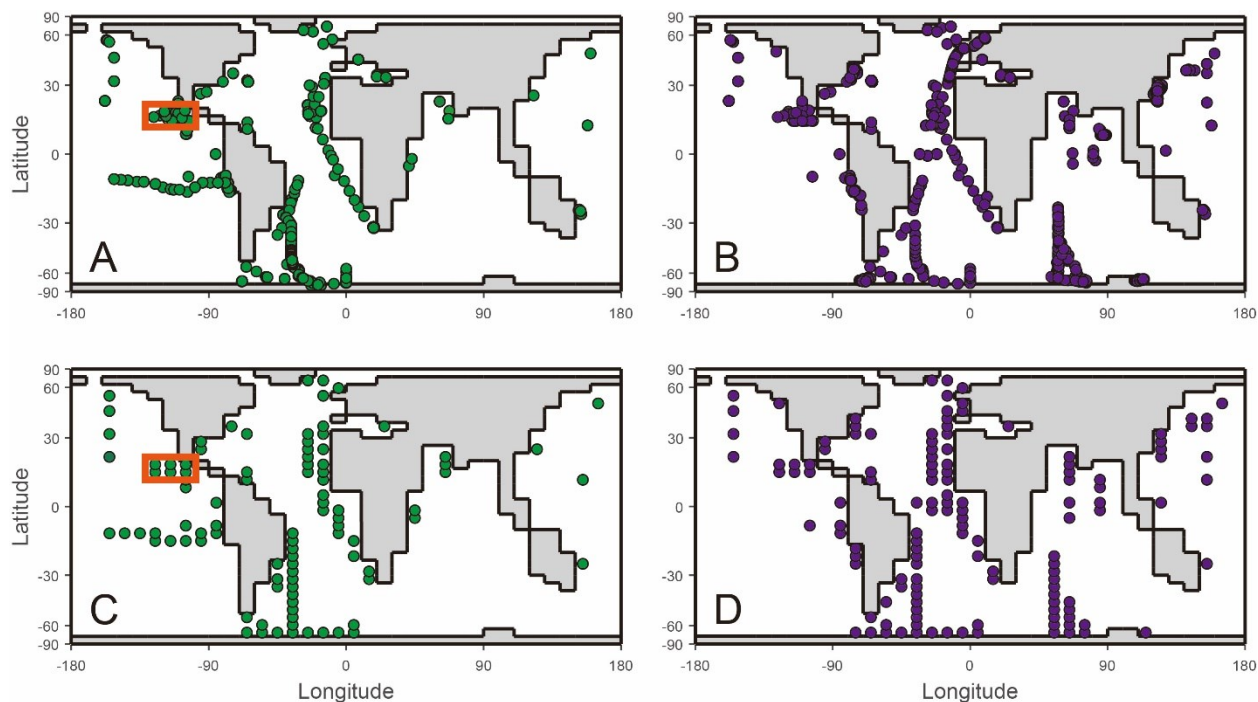
Figure 2: Ocean surface (uppermost ~81 m corresponding to the depth of the surface layer in the cGENIE model) sampling locations of IO$_3^-$ (A) and I$^-$ (B) field observations after data filtration for freshwater and sediment fluxes. The filtered observations were then gridded according to the cGENIE 36×36×16 framework for model-data comparison of IO$_3^-$ (C) and I$^-$ (D). The orange boxes in A and C highlight the grids of the oxygen deficient zone transect shown in Fig. 7.

2.4   Sensitivity analyses and model implementation

Because the relative roles of IO$_3^-$ reduction, I$^-$ oxidation, and the shuttling of iodine through the biological pump are uncertain, we calibrate the parameters controlling these processes in cGENIE by creating an ensemble of different parameter value combinations controlling IO$_3^-$ reduction and I$^-$ oxidation in a 2D regularly spaced grid and then repeat the same 2D parameter ensemble for different assumptions regarding the biological pump (I:C) (Table 1, Fig. 4). We focus on parameter ensembles testing the 3 different parameterizations for I$^-$ oxidation (but only 'threshold' as the IO$_3^-$ reduction parameterization) – 'lifetime-threshold', 'fennel-threshold', and 'reminO2lifetime-threshold'. (The results of 2 additional parameterization-combinations – 'lifetime-reminSO4lifetime', and 'lifetime-inhibition' are given in Table S1.) We discuss the reasons for selecting these specific parameterization-combinations in the Discussion section. Finally, to explore whether the cGENIE model-simulated dissolved oxygen distribution imparts any particular

252 bias to the tuned iodine cycle, we repeated the model ensembles for each of the 3 parameterization-combinations but

253 continually restoring the 3D pattern of $[O_2]$ in the model to that of the World Ocean Atlas 18 (WOA18) climatology

254 (Garcia et al., 2018). The model ensembles are summarized in Table 1.

255   Each ensemble member was run for a total of 2,000 years and each starts from the same initial state, which

256 was an experiment run for 10,000 years to equilibrium using a random set of iodine parameters within the ranges in

257 Table 1. Running each ensemble member for 2000 years minimizes the CPU time but was also found to be more than

258 sufficient to allow iodine inventories to equilibrate to new steady states. The output of each ensemble member is then

259 statistically compared to our observational database.

260

261 **2.5   Evaluation against geological observations**

262 Parameter tuning, and the ability to reproduce modern observations, does not by itself offer any guarantee that spatial

263 patterns are being simulated for the 'correct' mechanistic reason. This is even more pertinent in the context of the

264 application of a modern-tuned model to paleoredox reconstruction. To quantify to what degree the calibrated

265 parameterization-combinations for the modern marine iodine cycle have predictive power in the geological past, we

266 carried out a deep-time plausibility test.

267   For the paleo plausibility test, we adopted the Cretaceous, pre-OAE2 (ca. 93 Ma) configuration (continental

268 arrangement and ocean bathymetry, wind stress and velocity, and zonal average planetary albedo boundary conditions)

269 of Monteiro et al., (2012). We choose this particular geological interval because the controls on ocean redox have

270 been previously evaluated using the cGENIE model (Monteiro et al., 2012; Hülse et al., 2019), the oceanic conditions

271 are much more extensively dysoxic and anoxic than present-day and hence represent a relatively severe test of the

272 model iodine cycle, and a number of I/Ca proxy measurements are available (Zhou et al., 2015). In order to evaluate

273 the same configuration of the iodine cycle as optimized in this study, we also substituted the temperature-independent

274 representation of biological export production and fixed remineralization profile of POM in the water column (i.e.,

275 Ridgwell et al., (2007)) for the temperature-dependent scheme of Crichton et al., (2021) used in our modern calibration.

276 However, in substituting the biological pump scheme in the model we alter the ocean redox landscape compared with

277 Monteiro et al., (2012). We therefore explore a range of different assumptions regarding the ocean PO_4 inventory at

278 the time as a means of generating a range of different plausible states of ocean oxygenation. In this, we test: 0.2, 0.4,

279 0.6, 0.8, 1.0, and 1.5 times the mean modern concentration (2.15 μM). We run the model with each of the best-fit

280 (highest M-score) sets of parameter values associated with the main 3 different parameterization-combinations (2

281 additional parameterization-combinations were run and are presented in SI), and for each of the varying PO_4 inventory

282 assumptions, and for 10,000 years to steady-state. Major cation concentrations were adjusted to a value more

283 representative of the earlier Cenozoic (18.2 mM $[Ca^{2+}]$, 29.9 mM $[Mg^{2+}]$) (Panchuk et al., 2008) although that does

284 not affect the calculation of carbonate I/Ca values. In the absence of independent constraints on the Cretaceous total

285 dissolved iodine inventory, we assumed this to be modern (500 nM mean concentration).

286

287
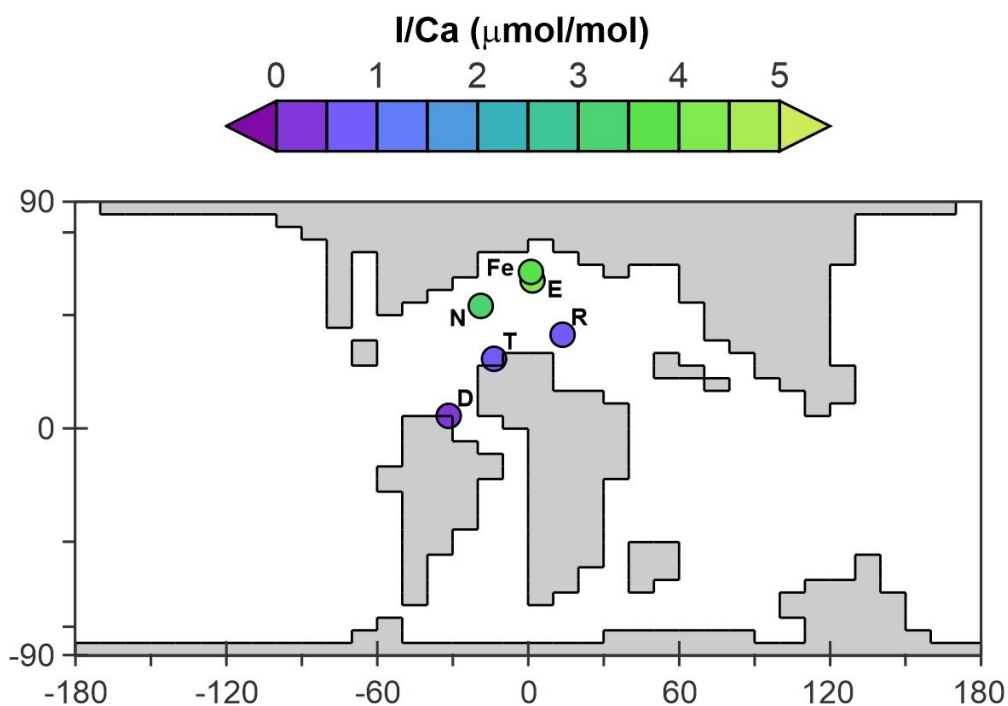
Figure 3: The continental setting during the Cretaceous OAE2 (Cenomanian - Turonian) in cGENIE. The colored dots represent averaged pre-OAE2 I/Ca measurements from each of the sections. D = Demerara Rise; E = Eastbourne; Fe = South Ferriby; N = Newfoundland; R = Raia del Pedale; T = Tarfaya.

288

289   The I/Ca data used for comparison with the model come from 6 sections (Zhou et al., 2015, Fig. 3, listed in

290   Table S3). The pre-OAE2 I/Ca baseline value from each section is estimated through averaging the pre-CIE I/Ca

291   measurements from Table S1 of Zhou et al., (2015). Diagenesis of carbonate hosted I/Ca tends to lower the primary

293   values (Hardisty et al., 2017). However, such an offset is hard to quantitatively predict based on our current knowledge.

294   In addition, according to Zhou et al., (2015), from which we adopted the I/Ca data, most of the sections only suffered

295   minor diagenesis. To simplify the Cretaceous I/Ca-to-IO_3 conversion, we regard the measured I/Ca as primary and

296   acknowledge there is potential uncertainty. For quantitative comparison between the model and the I/Ca data, we

297   create an empirically derived forward proxy model for I/Ca. In this, we took the simulated concentration of IO_3^- and

298   Ca^{2+} in the ocean surface layer of the model at every ocean grid point, and applied the temperature-dependent linear

299   incorporation relationship derived from inorganic calcite synthesis experiment of Zhou et al., (2014), to estimate I/Ca.

300   Specifically, the distribution coefficient (K_D) between I/Ca and $[IO_3]$ (K_D = (I/Ca)/ $[IO_3]$) shows linear dependency

301   with temperature (Fig. S3 in Zhou et al., 2014). For our Cretaceous model calibration, we apply the K_D based on local

302   temperature (at each grid point associated with a sampling section) simulated by cGENIE. Beyond temperature, we

303   acknowledge that IO_3^- incorporation into carbonate lattice through substitution $IO_3^- + Na^+ \leftrightarrow CO_3^{2-} + Ca^{2+}$ is controlled

304   by $[Na^+]$, $[CO_3^{2-}]$, and $[Ca^{2+}]$ (Podder et al., 2017). However, either quantifying these ions during the Cretaceous

305   seawater or quantitative calculation of ion substitution dynamics requires further constraints. Although uncertainties

309   are inevitable, we assume our temperature-controlled [IO₃⁻]-to-I/Ca conversion based on current quantitative

310   knowledge meets the requirement for Cretaceous model-data comparison. We extracted simulated I/Ca values from

311   the model grid points corresponding to the sections reported by Zhou et al., (2015) and calculated the M-score.

312

313

314
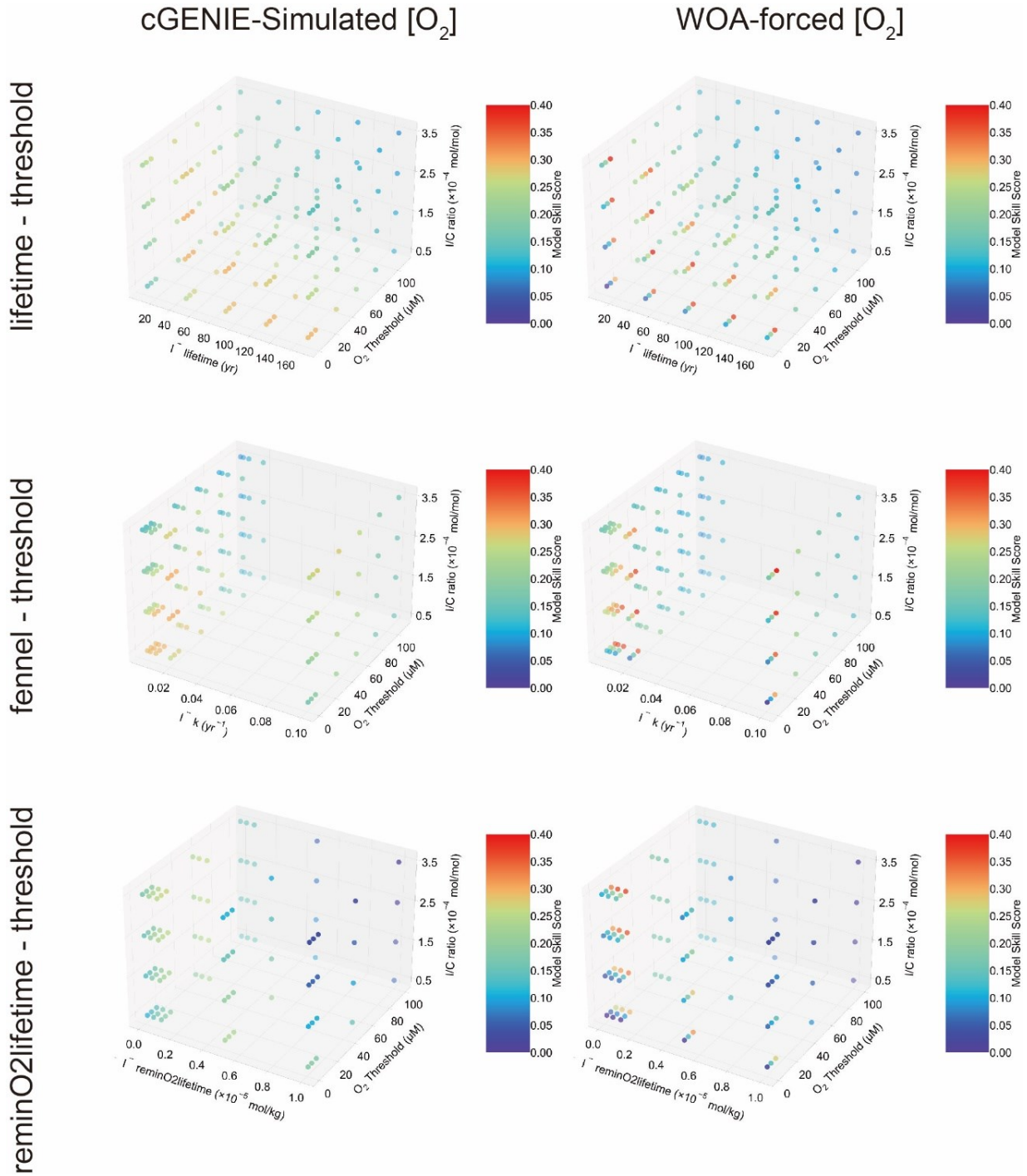
Figure 4: The three-dimensional model skill score array of the experiment ensembles.

318 **Table 1. The cGENIE iodine redox options and the associated range of parameters of these options.**
319 **The detailed introduction of each parameter is described in section 2.2.2 and the plausibility of these parameter**
320 **ranges is discussed in 4.1.1. Note that the oxidation rate constant k in 'Fennel' is in unit of year^{-1} in the model**
321 **configuration, which is the reciprocal of the 'lifetime'. A detailed table containing all considered**
322 **parameterization ranges can be found in Table S1.**

Parameterization-combination		Iodine oxidation parameters			Iodine reduction parameters	I:C ratio (× 10^{-4} mol/mol)
		'lifetime' (years)	'reminO2lifetime' (× 10^{-5} mol/kg)	'Fennel' (Inhibition constant/ μM O_2)	'threshold' (μM O_2)	
'lifetime-threshold'	cGENIE O_2	10-170	\	\	1-110	0.5-3.5
	WOA	10-170	\	\	1-110	0.5-3.5
'fennel-threshold'	cGENIE O_2.	10-170 (1/k)		20	1-110	0.5-3.5
	WOA.	10-170 (1/k)		20	1-110	0.5-3.5
'reminO2lifetime-threshold'	cGENIE O_2	\	0.01-1	\	1-100	0.5-3.5
	WOA	\	0.01-1	\	1-100	0.5-3.5

3. Results

In this section, we start by summarizing the overall statistical outcome of the tuning, then present a series of spatial analysis comparisons for each of the highest M-score ensemble members. The spatial analyses progressively reduce in scale, moving from global surface distributions (Section 3.2), to global and basin-specific water column profiles (Section 3.3), and finally to spatial comparisons for a specific ODZ region (Section 3.4). Our final set of results (Section 3.5) are of the modeled Cretaceous scenarios using the best parameterizations from the modern, which then are compared to carbonate I/Ca values measured in the rock record.

3.1. Model skill score

The M-score values achieved across the complete ensemble for each of the 3 main parameterization-combinations are shown in Fig. 4 and illustrate how the statistical fit is M-score sensitive to all three of the main parameters. Higher model skill scores are usually reached when 'threshold' is tuned to 10 μM [O_2] for all the ensembles, including both model-simulated [O_2] and WOA-forced [O_2]. For the ensembles, 'lifetime-threshold' and 'fennel-threshold', the highest M-scores are similar – 0.305 and 0.308, respectively (Table 2). Both these ensembles have the highest performance when 'threshold', 'lifetime', and I:C ratio are tuned to 10 μM [O_2], 50 years, and 1.5×10^{-4} mol/mol, respectively, which is generally consistent with observations (Lu et al., 2016, 2020b; Tsunogai, 1971; Elderfield and Truesdale, 1980) (discussed in more detail later). The model performance of 'reminO2lifetime-threshold' is less good than the other two combinations, with the best M-score of 0.266 when 'threshold', 'reminO2lifetime', and I:C ratio are tuned to 10 μM O_2, 1×10^{-6} mol/kg, and 3.5×10^{-4} mol/mol, respectively (Table 2, Fig. 4). We note that for each parameterization-combination, the highest possible M-score achievable by tuning improves when [O_2] is forced to that of the World Ocean Atlas 18 (WOA18) climatology (Garcia et al., 2018).

3.2. Meridional surface I⁻ distribution

Figure 5 shows a comparison between the observed latitudinal distribution of [I⁻] at the surface and as simulated by the model for each parameterization-combination (for the respective best M-score ensemble member). Note that the observations (Section 2.3) are binned to the corresponding model grid cells and as such, reflect averages over the upper-most 80 m of the water column. This represents a reduction from 1338 to 141 surface ocean data points. We find that the surface ocean [I⁻] in the model shows a trend of increasing values towards low latitudes, broadly consistent with observations (Chance et al., 2014) (Fig. 5). The 'lifetime-threshold' and 'fennel-threshold' show similar latitudinal trends, but both overestimate the surface I⁻ in the mid-low latitudes in the southern hemisphere. The 'reminO2lifetime-threshold' ensemble produces better estimation of meridional surface [I⁻] trend, although overestimates [I⁻] in the tropical surface ocean compared to the other two ensembles (Fig. 5).
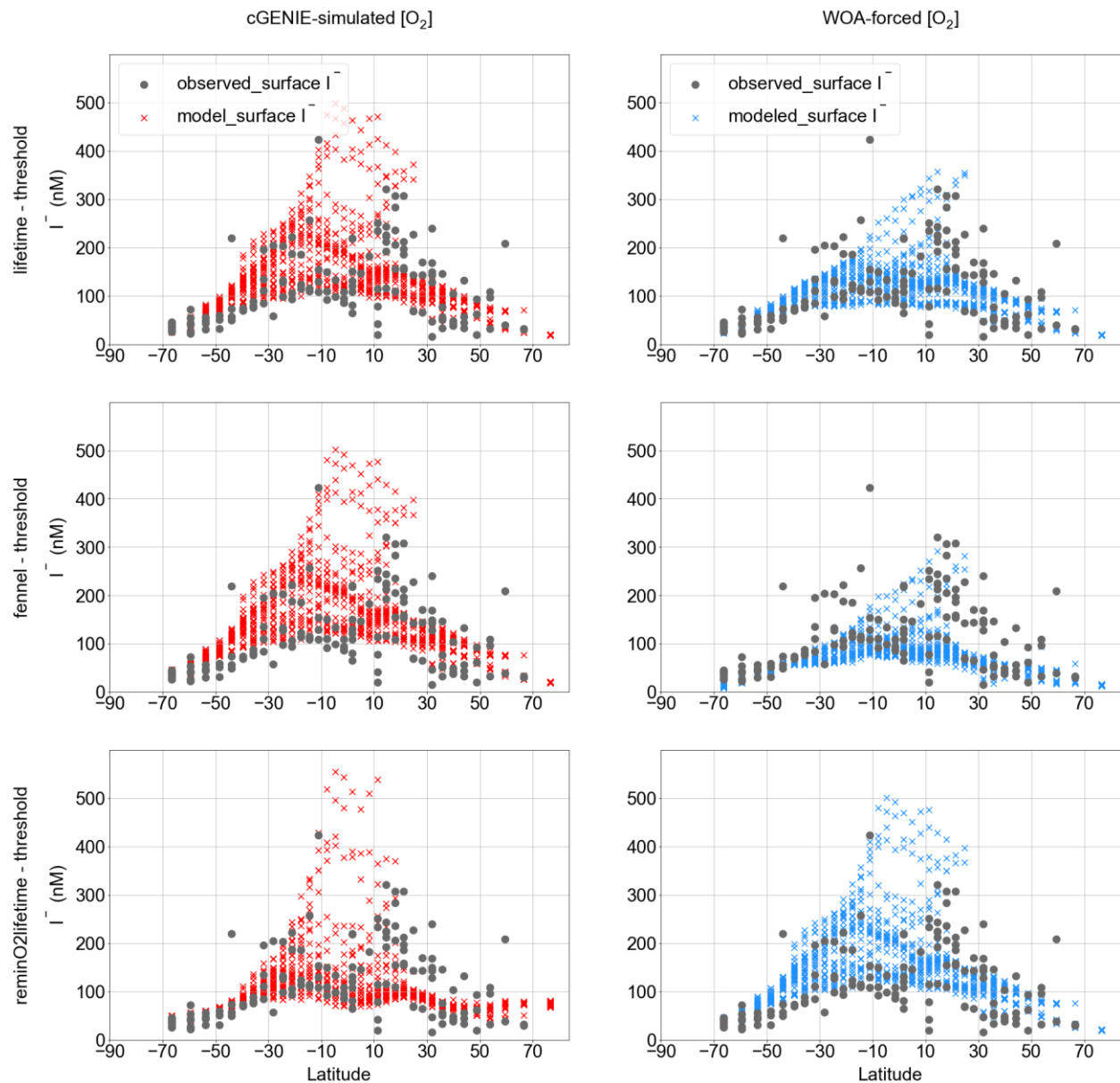
Figure 5: Modeled latitudinal surface iodide distribution compared with observation with the cGENIE simulated [O₂] and the [O₂] restoring forcing. The elevated [I⁻] observed and modeled in low latitudes is the result of phytoplankton reduction in the surface ocean. Note that the I⁻ distribution simulated by 'lifetime-threshold' and 'fennel-threshold' are close but not identical.

3.3. Global and basin-specific iodine depth distributions

Comparisons between the observed distributions of I⁻ and IO₃⁻ seawater concentrations among the global ocean and the Atlantic and Pacific Oceans are presented in Fig. 6. Again, we gridded the iodine observations (see: Section 2.4) and selected sub-sets of the data that lay in either Atlantic or Pacific basins, contrasting with the corresponding model values at those locations. We find only relatively minor differences between the best M-score ensemble member of

each of all three parameterization-combinations, and all show increased $[IO_3^-]$ and decreased $[I^-]$ with increased depth below the euphotic zone in the Atlantic and Pacific basins, as well as globally (Fig. 6). The modeled depth profile broadly matches with observation in the Atlantic and deep Pacific Ocean, except the underestimated subsurface peak of $[I^-]$ observed in the Pacific and overestimated $[IO_3^-]$ in the deep Pacific (Fig. 6). This mismatch of subsurface I^- peak is probably the result of sampling bias, with most of the Pacific iodine observations from ODZs in the Eastern Tropical North Pacific (ETNP) and the Eastern Tropical South Pacific (ETSP). For example, in model depth profiles masked to only include grid points with corresponding observations, the modelled Pacific depth profiles show a clear mid-depth ODZ feature (Fig. S9).
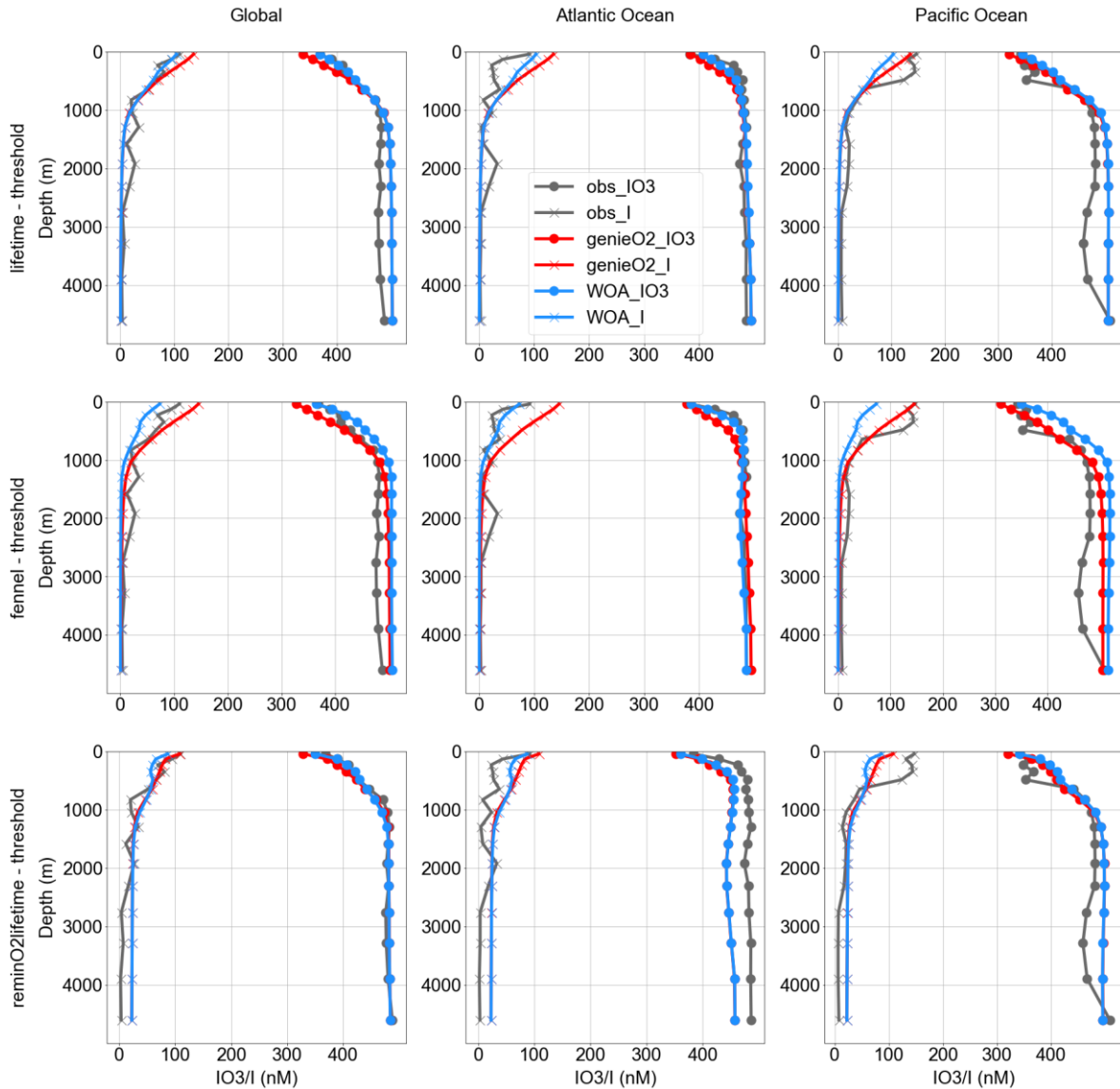

Figure 6: Modeled averaged iodine (including iodate and iodide) depth profile among global ocean, the Pacific, and the Atlantic compared with observation. The surface I^- enrichment among the ocean basins is caused by phytoplankton reduction. The subsurface (~500m) I^- enrichment is the result of sampling bias since most of the observations are from the ETNP and ETSP ODZs (see main text for details).

15

380

3.4.   Iodine distribution within ODZs

382   To assess the model ability to simulate iodine cycling in marine low oxygen environments, we compared distributions

383   of oxygen and iodine species in the ETNP (Fig. 7). The O_2 transects amongst all model simulations are the same

384   because we only changed the parameterizations of the iodine cycle between ensembles and ensemble members (i.e.,

385   they all simulate the same biological pump in the ocean). All the three chosen best-performance-experiments show

386   similar iodine anomalies (IO_3^- depletion) in the ETNP, fitting the general feature of the observation. Other

387   parameterizations did not replicate the ODZ (Fig. S4). However, even under the "best-fitting" parameters, compared

388   to the observations, the ODZ feature in the model is underestimated both in intensity and in areal extent compared to

389   the observations (Fig. 7). Notably, compared to $[O_2]$ measured in the ETNP transect, the model underestimates the

390   extent of the ODZ. Severe deoxygenation below 50 µM $[O_2]$ was observed in relatively shallow depths between 100-

391   200m in the ETNP, and this ODZ extends for more than 3000 km towards off-shore from Mexican coast (Fig. 7).

392   Although cGENIE simulates the O_2-deficient pattern in the ETNP, the extent of the ODZ is underestimated. The

393   simulated oxycline is ~200 m deeper than the observation and the $[O_2]$ variation is gradual. The ODZ below 20 µM

394    $[O_2]$ in the model is limited to a small spatial extent within 1000 km offshore, which is much smaller than that in the

395   observation (Fig. 7).

396
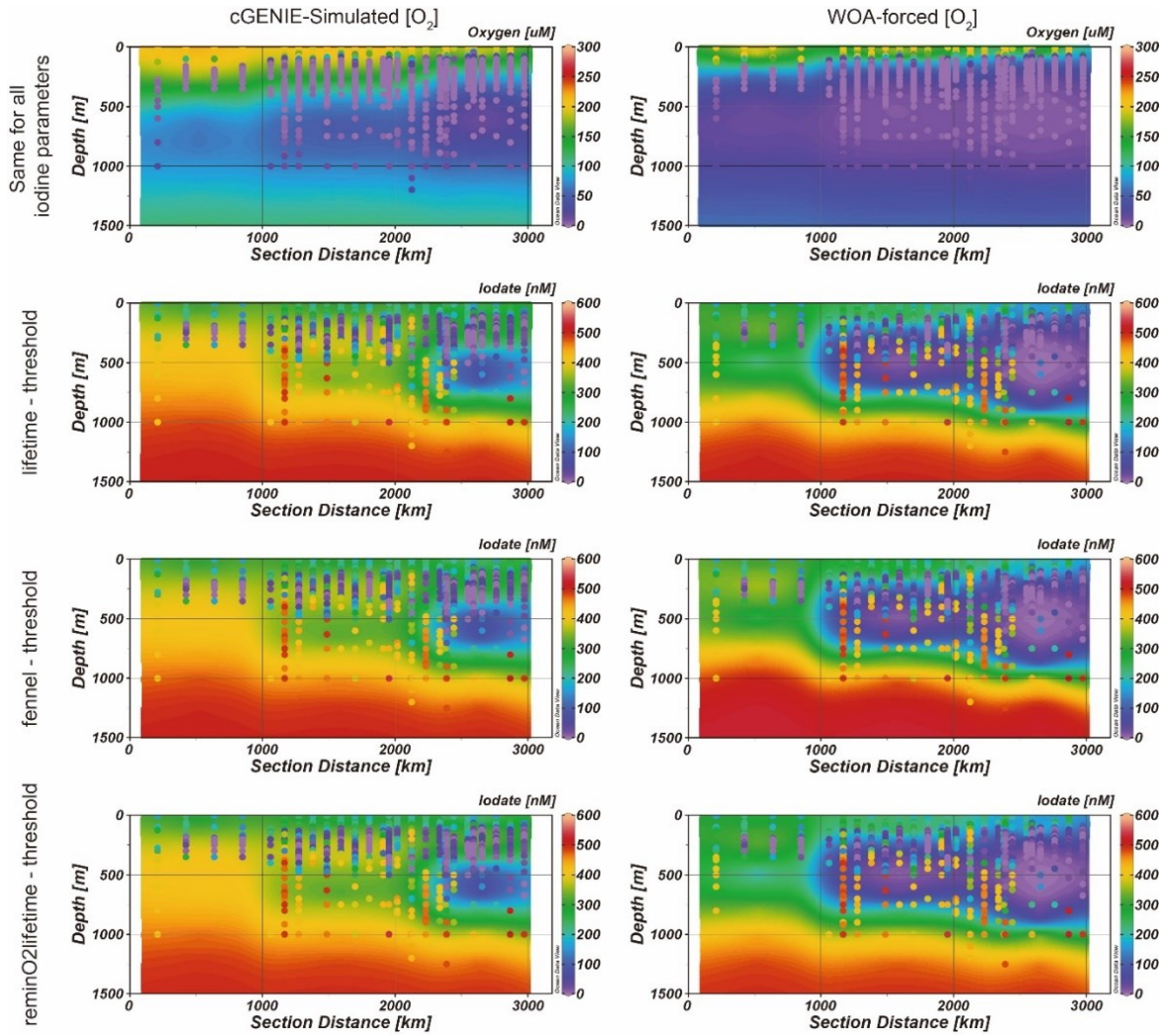
Figure 7: Modeled (contour) and observed (colored dots) west-to-east transect (location shown in Fig. 1) of O$_2$ (top row) and IO$_3^-$ (bottom rows) in the ETNP. Note that the WOA-forced [O$_2$] models simulate a larger extent of IO$_3^-$ anomaly, which better matches the observation. The left-hand panel contours are model results based on cGENIE-simulated [O$_2$] while contours on the right are model results from WOA-forced [O$_2$].

We also ran model ensembles forcing cGENIE to restore the modern ocean [O$_2$] annual average climatology to that of the WOA18 (Garcia et al., 2018) (Fig. 7). Under these conditions, the subsurface IO$_3^-$ depletion zone in the ETNP ODZ in all three ensembles extends ~2000 km offshore and spans across 100-1000 m in depth (Fig. 7). The shallow and extended ODZ iodine distribution in the ETNP better matches the observation compared to non-O$_2$ restoration simulations.

Table 2. The performance of the cGENIE iodine simulations and associated parameterization when the model reaches the best global M-score. Note that the oxidation rate constant *k* in 'Fennel' is in unit of year^{-1} in the model configuration, which is also the reciprocal of the 'lifetime'. The full model performance is summarized in Table S2.

17

Parameterization-combination		Iodine oxidation parameters			Iodine reduction parameters	I:C ratio (× 10^{-4} mol/mol)	Model skill score
		'lifetime' (years)	'reminO2lifetime' (× 10^{-5} mol/kg)	'Fennel' (Inhibition constant/ μM O_2)	'threshold' (μM O_2)		
'lifetime-threshold'	cGENIE O_2	50	\	\	10	1.5	0.305
	WOA	50	\	\	10	1.5	0.385
'fennel-threshold'	cGENIE O_2	50 (1/k)	\	20	10	1.5	0.308
	WOA	10 (1/k)	\	20	10	3.5	0.385
'reminO2lifetime-threshold'	cGENIE O_2	\	0.1	\	10	3.5	0.266
	WOA	\	0.1	\	10	3.5	0.365

413

3.5   Evaluation against geological observations

415

416

417
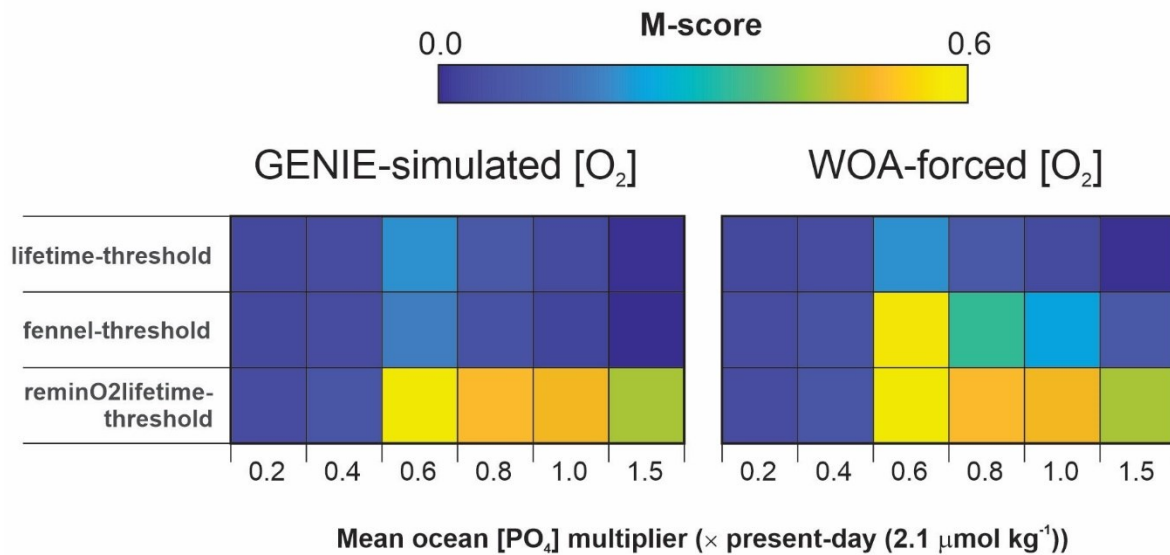
Figure 8. The model skill scores of modeled and measured I/Ca during the pre-OAE2. The iodine cycling parameters are derived from modern simulations with cGENIE-simulated [O₂] and WOA-forced [O₂], respectively.

421

The statistical results of the pre-OAE2 evaluation are illustrated in Fig. 8 for the 3 main parameterization-combinations

and for parameter calibrations derived from internally and WOA-forced dissolved oxygen distributions (and in Fig.

S10 for the full set of parameterization-combinations tested). Most of the parameterization-combinations reach their

18

425 highest M-scores under the assumption of 0.6-0.8 × modern [PO_4] (Fig. S10). Previous analysis using the same

426 climatological configuration of the cGENIE model indicated a PO_4 inventory of 1.0 x modern was most consistent

427 with geological redox-related observations prior to OAE2 (Monteiro et al., 2012). However, our assumption here of

428 temperature-dependent POM export and remineralization leads to higher export and shallower more intense ODZs

429 compared to temperature-invariant biological scheme (see: Crichton et al., (2021)). Hence, for a similar degree of

430 ocean anoxia, we would expect the need for a slightly lower nutrient inventory, as we indeed find.

431 In terms of the I/Ca M-score, we find the parameterization-combinations 'reminO2lifetime-threshold' and

432 'fennel-threshold' better replicate the geological observations compared to the 'lifetime-threshold'. For 'fennel-

433 threshold', the WOA-derived parameter set values differ from those derived from cGENIE-[O_2] (Table 2) and perform

434 better. The performance of the scheme 'reminO2lifetime-threshold' is largely independent of the ocean PO_4 inventory

435 assumption for values of 0.6 × modern and higher.

4.   Discussion

437 In summary: we presented the results of cGENIE Earth system model ensembles (both with internally calculated and

438 WOA-imposed [O_2] distribution) for 3 parameterization-combinations of iodine cycling that showed the best

439 performance (but summarize a total of 5 different parameterization-combinations in Table S2). We analyzed the

440 performance of the ensembles via: (1) M-score for the model-data match of both [I^-] and [IO_3^-] across the entire ocean,

441 (2) qualitative model-observation comparison of latitudinal surface ocean distributions of [I^-], (3) inspection of

442 averaged depth profiles in global and individual ocean basins for both [I^-] and [IO_3^-], (4) inspection of iodine transects

443 across the across the Eastern Tropical North Pacific (ETNP) ODZ, and (5) M-score for model and carbonate I/Ca

444 observations (Zhou et al., 2015) for the Cretaceous.

4.1.   Overall model skill score comparison

446 Two broad observations emerge from the M-score comparison. First, the 1st-order kinetic iodine oxidation

447 associated ensembles ('lifetime-threshold' and 'Fennel-threshold') have the highest M-scores (Table 2), under both

448 cGENIE-simulated [O_2] and WOA-forced [O_2]. This is consistent with previous observations of 1st-order kinetics for

449 I^- oxidation (Tsunogai, 1971). Second, the simulations with WOA-forced [O_2] produce significantly higher M-

450 scores than that of the cGENIE-simulated [O_2] field (at least ~0.08 of improvement; Table 2). Despite a 1st-order

451 non-O_2 dependent oxidation mechanism providing the highest M-scores, the WOA vs internally model-generated

452 dissolved oxygen distributions comparison highlights the O_2 and related redox dependency of the iodine cycle from

453 the perspective of IO_3^- reduction. Each of these factors are discussed in the following Section 4.1.1.

4.1.1.   Parameter value plausibility

455 A credible representation of the marine iodine cycle requires not only that observations can be replicated, but that in

456 achieving a fit to observations, tuned parameter values fall within real-world ranges. In this section, we discuss the

457 plausibility of our best-fit (maximized M-score) parameter values. For the iodine cycle, these parameters are: the O_2

458   threshold, the parameter (depending on the specific parameterization-combination) controlling the I⁻ oxidation rate,

459   and the cellular I:C ratio.

460   Our model M-score is highest with an [O_2] reduction threshold of 10 µM (Fig. 4 and Table 2). Although it is

461   generally well accepted that IO_3^- is reduced in low oxygen settings (Luther, 1991; Rue et al., 1997; Wong et al., 1985;

462   Wong and Brewer, 1977; Farrenkopf and Luther, 2002), the degree of O_2 depletion that triggers IO_3^- reduction is still

463   unclear. A relatively high threshold for triggering IO_3^- reduction has been proposed based on comparison between

464   planktic and benthic foraminiferal I/Ca and ambient [O_2] (20-70 µM O_2; Lu et al., 2016, 2020a). These [O_2] thresholds

465   are similar to that determined in a previous cGENIE-based iodine cycle study (30 µM) (Lu et al., 2018), but it is

466   difficult to directly compare this to our results because of differences in the model representation of the ocean

467   biological pump, the iodine observational dataset, and model-data comparison methods utilized.

468   Many of the studies suggesting a relatively high [O_2] threshold are based on the relationship of [IO_3^-] and

469   [O_2] within the upper chemocline of ODZs; however, evaluation of [O_2] and [IO_3^-] from ODZs throughout the entire

470   water column suggest the potential for IO_3^- persistence within the low oxygen cores of ODZs. Specifically, IO_3^-

471   accumulation is observed within the ETNP and ETSP at depths where [O_2] is close to or below the detection limit of

472   the sensors which is reported near 1 µM (Hardisty et al., 2021). In addition, it is worth noting that the kinetics of IO_3^-

473   reduction is heterogeneous both within and between ODZs. For example, a transect evaluating IO_3^- reduction rates in

474   the ETNP observed rapid rates in the upper oxycline, where [O_2] was near ~12 µM, but the potential for sluggish rates

475   in the ODZ cores, where [O_2] was below detection. In an early study of the Arabian Sea, IO_3^- was reduced rapidly

476   within the ODZ core. Together, these suggest IO_3^- reduction may be controlled by factors beyond O_2 (Hardisty et al.,

477   2021; Farrenkopf and Luther, 2002). For example, IO_3^- is likely formed in high [O_2], non-ODZ water masses but can

478   be sustained upon transport or mixing within oligotrophic, offshore ODZ regions where organic supplies are more

479   limited (Hardisty et al., 2021). A comparison to the N cycle would also indicate a low [O_2] threshold – for example,

480   denitrification has a sub-µM [O_2] threshold and has a similar redox potential with IO_3^- reduction (Dalsgaard et al.,

481   2014; Thamdrup et al., 2012). A sub-µM [O_2] threshold for IO_3^- reduction could explain the [IO_3^-] variations observed

482   in ODZ cores with [O_2] below the µM detection limits of sensors; however, iodine speciation has yet to be analyzed

483   alongside [O_2] measurements via sensors with sub-µM detection limits, such as STOX sensors. Regardless, our 10

484   µM [O_2] threshold based on maximizing the M-score reflects a global average value and clearly falls within the ranges

485   of oceanographic observations.

486   For both our study and that of Lu et al., (2018), an I⁻ lifetime of 50 years maximizes model performance.

487   However, Lu et al., (2018) chose to implement a slightly lower value of 40 years for their paleo-application because

488   it reflected the slowest rate observed in the literature at that time (Tsunogai, 1971). Notably, though IO_3^- is the most

489   abundant marine iodine species, its production from I⁻ has never been unambiguously observed under normal marine

490   conditions. This has acted as a major hinderance on providing direct constraints. That said, our model-based estimate

491   is consistent with a multitude of other constraints that indicate that I⁻ oxidation to IO_3^- undergoes extremely slow

492   kinetics. The I⁻ oxidation rates calculated through indirect methods including mass balance and seasonal iodine

493   speciation changes (Tsunogai, 1971; Campos et al., 1996; Truesdale et al., 2001; He et al., 2013; Edwards and

494   Truesdale, 1997; Žic et al., 2013; Moriyasu et al., 2023) or through radiogenic tracer spiked incubations (Hardisty et

495   al., 2020; Schnur et al., 2024; Ştreangă et al., 2024) have a wide range of variation from 1.5 nM/yr to 670 nM/yr. The

496   lifetime in cGENIE is 50 years, which can be approximately converted to the zeroth order rate of <9 nM/yr, falling in

497   the lower end of the previous studies.

498   Our best-fit I:C ratio is 1.5×10^{-4} mol/mol, which is in agreement with plankton measurements and mass-

499   balance calculations (Chance et al., 2010; Elderfield and Truesdale, 1980). In the euphotic zone, IO_3^- is taken up by

500   phytoplankton and incorporated into their cellular structures followed by subsequent conversion into I^- (Hepach et al.,

501   2020). Due to this, it is assumed that IO_3^- removal in the surface layer of the ocean is a function of organic carbon

502   fixation during primary productivity according to Redfield-like ratios (Campos et al., 1996; Chance et al., 2010). Of

503   the parameters incorporated into the model, in theory, I:C should probably be the best constrained. However, published

504   I:C ratios based on field and laboratory measurements vary over several orders of magnitude (10^{-5} to 10^{-3}) (Elderfield

505   and Truesdale, 1980; Campos et al., 1996; Hepach et al., 2020; Chance et al., 2010). To limit the number of model

506   simulations and size of the ensembles, we only varied I:C between 5×10^{-5} and 3.5×10^{-4} mol/mol (in increments of

507   1.0×10^{-4}), which covers the range indicated by previous studies (Elderfield and Truesdale, 1980).

508   It is unlikely that the I:C value is constant across the global ocean due to differences in phytoplankton

509   composition and other factors, such as temperature (Wadley et al., 2020). In cGENIE, most of the elevated (> 200 nM)

510   surface $[I^-]$ values occur in the ETSP and the northern Indian Ocean, representing the effect of high primary

511   productivity and transformation of IO_3^- to I^- via the rapid recycling DOM 'loss term' in the representation of biological

512   export in the model (Fig. S6). The overestimation of tropical I^- within the model probably hints that the I:C ratio is

513   not constant in the ocean, as which is also hypothesized by Wadley et al., (2020), although in the absence of an explicit

514   representation of primary productivity in the model and spatially variable f-ratios (Laws et al., 2000) (implicitly, the

515   f-ratio can be considered to be 0.33 everywhere in cGENIE). In testing a fixed, spatially uniform I:C, Wadley et al.

516   (2020) underestimated surface $[I^-]$ in low latitudes and overestimated concentrations in mid-latitudes. Based on their

517   model-observation comparison, they hypothesized that the I:C ratio decreases systematically with sea surface

518   temperature (SST) (Wadley et al., 2020). Until more constraints are developed on spatial variability and associated

519   driving factors for I:C, a generalized approach of a globally uniform I:C remains the most parsimonious assumption,

520   especially considering cGENIE's intended extrapolation to ancient settings.

521   **4.1.2.   Comparing alternative iodide oxidation parameterizations in cGENIE**

522   Due to similarity in redox potentials, iodine cycling in the ocean has been hypothesized to be linked to the cycling of

523   nitrogen (Rue et al., 1997). Nitrification promoting I^- oxidation to IO_3^- has been inferred from field studies (Truesdale

524   et al., 2001; Žic et al., 2013), and more recently has been linked via observation of I^- oxidation to IO_3^- by ammonia

525   oxidizing bacteria in laboratory environments (Hughes et al., 2021). We further note that Wadley et al., (2020)

526   explicitly link I^- oxidation to NH_4^+ oxidation in their surface ocean iodine cycle model.

527   As an alternative to the first-order lifetime oxidation parameterization used here and in Lu et al., (2018) and

528   in the current absence of a full nitrogen cycle (and hence explicit NH_4^+ oxidation) in cGENIE, we also applied a

529   strategy ('reminO2lifetime') which links I^- oxidation to organic carbon remineralization and the consumption rate of

530   dissolved oxygen. The reasoning behind this is that the O_2 consumption rate in the model implicitly reflects bacterial

531   oxidizing activity in the water column and hence the potential for I$^-$ to be oxidized to IO$_3^-$. We find that the overall

532   model performance involved with the 'reminO2lifetime' is lower than other experiments where I$^-$ oxidation is

533   ubiquitously oxidized according to a parametrized lifetime, or 'lifetime-threshold' (maximum M-score 0.266 vs.

534   0.305/0.308 under cGENIE simulated [O$_2$]) (Fig. 4 and Table 2). However, despite slightly lower M-scores, the

535   'reminO2lifetime' scheme generally replicates the latitudinal surface [I$^-$] trend, the depth profiles in the ocean basins,

536   and the ODZ transect (Figs. 4-6).

537   Under the default 'lifetime' scheme, I$^-$ will oxidize in the whole ocean regardless of the concentration (or

538   even presence/absence) of ambient O$_2$. This scenario might hence not perform well in replicating the ocean iodine

539   cycling at intervals during the Phanerozoic when ODZs were highly expanded, as it does not account for the possibility

540   for slower I$^-$ oxidation at low O$_2$ but above the IO$_3^-$ reduction O$_2$ threshold. Ideally, for application in

541   paleoceanographic studies, I$^-$ oxidation should be linked to ambient [O$_2$] in some way. Although thermodynamics

542   theory suggests O$_2$ does not directly drive I$^-$ oxidation (Luther et al., 1995), field studies in ODZs indeed observed

543   low [O$_2$] inhibits this process (Farrenkopf and Luther, 2002; Moriyasu et al., 2020). We hence developed and tested

544   variable I$^-$ oxidation kinetics, with the ambient dissolved O$_2$ providing an inhibition of the rate of oxidation based on

545   the enzymatic nitrification scheme of Fennel et al., (2005).

546   Since most of the ocean is fully oxygenated today, there is little difference in M-scores between 'lifetime' and

547   'Fennel' oxidation parameterizations (0.305 vs. 0.308, Table 2). Despite the very close M-scores, 'Fennel' oxidation

548   under WOA-forcing has a higher optimal I:C ratio (3.5 × 10^{-4} mol/mol) and faster saturated I$^-$ oxidation kinetics (0.1

549   yr^{-1} vs. 0.02 yr^{-1} in other ensembles). Such parameter differences between 'Fennel'-WOA and other ensembles reflect

550   compensation between faster oxidation rate (process (2) in Fig. 1) and increased I$^-$ production through the higher biotic

551   uptake rate (process (3) in Fig. 1). The pre-OAE2 simulations are particularly illustrative of this tradeoff and are

552   discussed in more detail in section 4.3.

553   In summary, all the three parameterization-combinations produce high and comparable M-scores and similar

554   parameters (oxidation, reduction, and I:C) associated with these M-scores (Table 2). Although direct field-based

555   evidence to evaluate the controlling parameters of 'reminO2lifetime' is absent, the parameters controlling the other

556   model scheme are consistent with previous studies.

557   **4.2.   Beyond the M-score: model-data comparison across iodine gradients**

558   As applied here, the M-score provides a quantitative measure that describes the overall model global performance and

559   allows us to directly compare the implications of parameter value and parameterization choices. However, a M-score

560   based on a global dataset can obscure regional gradients that may be important for both paleo- and modern

561   oceanographic research. Indeed, amongst all the various ensembles we ran as part of this study (Table S1), only

562   'lifetime-threshold', 'lifetime-Fennel', and 'reminO2lifetime-threshold' performed sufficiently well in replicating the

563   modern oceanic iodine gradients (Figs. S2-S4) and we thus decided to focus only on these 3 parameterization-

564   combinations. We now discuss this in more detail below.

565   **4.2.1.   Meridional surface [I$^-$] gradient**

566   All the 3 main parameterization-combinations summarized in Table 2, as well as the observations, show enrichment

567   of I⁻ in the surface ocean at low latitudes (Fig. 5). The pathway of transforming IO_3^- into I⁻ in these oxidized waters is

568   through primary productivity in the euphotic zone, which results in I⁻ accumulation within the mixed layer (Chance et

569   al., 2014). In the low latitudinal surface ocean, weaker vertical mixing resulting from warmer surface temperatures

570   allows I⁻ accumulation in the shallow mixed layer (Chance et al., 2014; Moriyaus et al., 2023). Therefore, the IO_3^- flux

571   from deep waters through seasonal mixing may be an important balance to *in situ* IO_3^- reduction rate by primary

572   producers in the high latitudes (Chance et al., 2014; Moriyasu et al., 2023). Importantly, this temperature stratification

573   and related vertical mixing trend is also simulated by cGENIE (Fig. S7). The cGENIE model generates the general

574   pattern of latitudinal surface I⁻ distribution pattern as well; however, overestimation especially in low latitudes may

575   exist, especially in the tropical surface where [I⁻] is close to 500 nM among all the cGENIE-O_2 models (Fig. 5).

576   The cGENIE (internally generated oxygen distributions) vs WOA (imposed distributions) O_2 comparison

577   provides evidence that I⁻ generated in low [O_2] settings may broadly enhance [I⁻] in oxygenated euphotic waters, with

578   lower and closer-to-observations [I⁻] values in the WOA tunings (Fig. 5). This includes 'lifetime-threshold', where O_2

579   only impacts the reductive portion of the iodine cycle, but also the 'Fennel' and 'reminO2lifetime' where rates of I⁻

580   oxidation are also [O_2] dependent. More specifically, most of the elevated (> 200 nM) surface [I⁻] in cGENIE, occurs

581   in the ETSP and the northern Indian Ocean and corresponds to locations of high primary productivity (Fig. S6). Since

582   the surface ocean [O_2] in the model is never below 200 μM, O_2-dependent IO_3^- reduction at the ocean surface is

583   unlikely. Instead, *ex situ* transport from proximal regions of subsurface anoxia is the most probable source of elevated

584   I⁻. Indeed, the most prominent regions of I⁻ enrichment in the model occur near the Peruvian coast and in the Arabian

585   Sea, where ODZs lie below the surface (Fig. S6). More detailed data-model comparison among these two areas is

586   limited because the observation data are few (e.g., Farrenkopf and Luther, 2002 and Rapp et al., 2020). In contrast,

587   the meridional trend of I⁻ in the surface Atlantic Ocean, where ODZs are less developed, exhibits better agreement

588   with both the observation and the Wadley et al., (2020) model (Fig. S6). The overestimation of tropical ocean surface

589   [I⁻] by cGENIE is hence likely to be associated with deficiencies in the simulation of ODZ oxygenation.

590   That said, modeled overestimations of surface ocean [I⁻] may be difficult to verify given current observational

591   data densities. In comparing observational data to model-latitudinal trends which have been masked to only include

592   model grid points with corresponding observations, although the same broad trend of increasing [I⁻] in the low latitudes

593   exists, there are fewer incidents of apparent model over-estimation (Fig. S8). More observations in surface ocean [I⁻]

594   from low latitudes are needed to better assess the validity of elevated modelled surface ocean [I⁻] in some regions.

595   **4.2.2.   Global and basin-specific iodine depth profiles**

596   All the iodine cycle schemes (both cGENIE-[O_2] and WOA-forced) generate a decrease in [I⁻] and increase in [IO_3^-]

597   from the euphotic zone down to the deep abyssal zone across ocean basins, matching the primary production-driven

598   pattern (Fig. 6). As discussed in the previous section, this surface maxima of [I⁻] in the oxygenated water column is

599   the result of biologically mediated reduction or release during cell senescence of phytoplankton. Below the euphotic

600   zone, [I⁻] is close to zero and IO_3^- becomes the dominant species. The deep ocean is mostly oxygenated and has longer

601   water residence times (several millennia, Matsumoto, (2007)) compared to the I$^-$ lifetime (<40 years, Tsunogai, (1971)),

602   thus facilitating I$^-$ oxidation in the absence of IO$_3^-$ reduction in ODZs.

603   We note that there are multiple general discrepancies between observations and model output as well as

604   differences between the results of WOA vs. cGENIE-[O$_2$] parameter tuning. In general, all models reproduce the

605   global average better, relative to the basin-specific profiles. We suggest that the global averaged profiles are a better

606   test of the cGENIE simulations because of sampling biases associated with individual basins. For example, the

607   discrepancy between the model and observations are prominent in the Pacific (Fig. 6). The observed Pacific subsurface

608   [I$^-$] peak mirrors the [IO$_3^-$] minima that occurs at depths where ODZs are present. This ODZ feature in the averaged

609   Pacific observation profile is likely the result of sampling bias since most of the observations from the Pacific are

610   from the ETNP (Rue et al., 1997; Moriyasu et al., 2020), and thus do not reflect the overall iodine distribution in the

611   Pacific Ocean (Fig. S9). This conclusion is supported by depth profiles masked to only include modeled grid points

612   with corresponding observation data. For example, there is a clear mid-depth ODZ feature in the masked model Pacific

613   depth profiles due to extensive ODZ studies in this region (Fig. S9). All this said, while the general features of iodine

614   speciation with depth are generally similar, our data compilation indicates the potential for some basin-specific

615   variations which require further research to validate and mechanistically understand.

4.2.3.   Iodine distribution within ODZs

617   One of the major goals of calibrating the iodine cycle in cGENIE is to be able to simulate the iodine behavior

618   associated with ancient low oxygen settings. To assess this potential, we analyzed model performance for the ETNP

619   (Rue et al., 1997; Moriyasu et al., 2020) where observational data are abundant and the areal extent of the ODZ is

620   sufficiently large to be reflected in the model grid (Fig. 6). The simulated reduction in IO$_3^-$ to I$^-$ generally overlaps

621   with the extent of the ODZ (Fig. 6), which provides support for the use of cGENIE to understand the broad distribution

622   of ancient [IO$_3^-$] and [O$_2$]. Non-threshold model parameterization-combinations (not discussed here but shown in Fig.

623   S4) did not replicate the ODZ feature in iodine speciation.

624   In all model configurations assuming cGENIE-[O$_2$], the most prominent discrepancy is an underestimation

625   of the spatial extent and intensity of the IO$_3^-$ depletion zone in the ETNP (Fig. 6) – a consequence of simulated

626   subsurface O$_2$ deficient area being notably narrower than WOA climatology (Fig. 6, Fig. S5). This is principally a

627   consequence of relatively weak continental margin upwelling and Equatorial divergence, itself a consequence of the

628   low resolution (both horizontally and vertically) model grid that the 3D ocean circulation component is implemented

629   on together with its simplified physics (Marsh et al., 2011). Another consequence of the low-resolution nature of the

630   cGENIE model grid is that the extent of the ETNP is of the order of the size of an individual grid box and the entire

631   ETNP only covers the longitude range of three grids in the model framework (Fig. 1). Meanwhile, the depth resolution

632   is ca. 100-200 m per layer in the upper ocean which also limits the finer simulation of ODZ features. Awareness of

633   these limitations highlights the importance of focusing use of the model on regional and global oxygenation features

634   as opposed to overinterpreting local features.

635   Other data-model misfits may be due to IO$_3^-$-reduction dependencies not explicitly accounted for in the model.

636   As discussed above, shipboard incubation and radiogenic-tracer-spiked rate calculation suggest that IO$_3^-$ reduction is

slow in the offshore ETNP ODZ (Hardisty et al., 2021). This could explain why measurable IO_3^- is present in the core of the ETNP ODZ (Fig. 6). This is further exacerbated in the Eastern Tropical South Pacific ODZ, where $[IO_3^-]$ remains above 250 nM in some studies (Cutter et al., 2018) but near detection limits in in others (Rapp et al., 2020), suggesting extreme spatiotemporal variability related to currently unconstrained factors. Further, while the capability of microbes using IO_3^- as an electron acceptor for oxidizing organic matter has been confirmed in laboratory culture experiments (Councell et al., 1997; Reyes-Umana et al., 2021; Yamazaki et al., 2020; Amachi et al., 2007; Farrenkopf et al., 1997), no study to date has demonstrated non-O_2 dependent controls driving variable IO_3^- reduction rates.

An important factor contributing to elevated $[I^-]$ in ODZs is benthic fluxes and reduction occurring within the uppermost layers of marine sediments (akin to denitrification). To help account for this in our M-score and model calibration (see: methods section), 'excess' iodine (>500 nM total iodine) was filtered from our observational dataset. The excess iodine originated from the sediment flux has been observed in ODZ water columns contacting anoxic sediments (Chapman, 1983; Farrenkopf and Luther, 2002; Cutter et al., 2018; Moriyasu et al., 2020; Scholz et al., 2024). We note that excess iodine occurs explicitly as I^-, reflecting the limited or lack of oxygen within the ODZ, and is a local-regional phenomenon not yet observed to persist beyond ODZ settings. Future work can focus on understanding the degree, if any, that excess I^- is oxidized to IO_3^-, and hence impacts the I/Ca paleoredox proxy.

4.3. Applicability of the cGENIE marine iodine cycle to paleoredox reconstruction

The pre-OAE2 comparison is revealing because the observations encapsulate a strong gradient between high and very low I/Ca (Fig. 3), reflecting respectively, high and low surface ocean concentrations of IO_3^- in the model. All three of the parameterization-combinations (just focusing on WOA-derived parameter values) are capable of reproducing low I/Ca values in the lower latitudinal sections (Demerara Rise, Tarfaya, and Raia del Pedale; Fig. 9), although with a tendency to slightly overestimate seawater IO_3^- depletion (cross-plots in Fig. 9). Low ocean surface $[IO_3^-]$ occurs in the model as a result of the existence of a circum-Equatorial band of intense sub-surface anoxia and short transport time to the surface (and hence limited oxidation). In the higher latitudinal sections, including Newfoundland, Eastbourne, and South Ferriby, I/Ca values tend to be underestimated to varying degrees (Fig. 9). However, compared to the 'lifetime' parameterization, both 'reminO2lifetime' and 'Fennel' oxidation simulate the I/Ca values in these high latitudinal sections rather better, with the regression closer to the 1:1 line (dotted in Fig. 9). We find this relationship instructional for understanding controls in the modern iodine cycle.
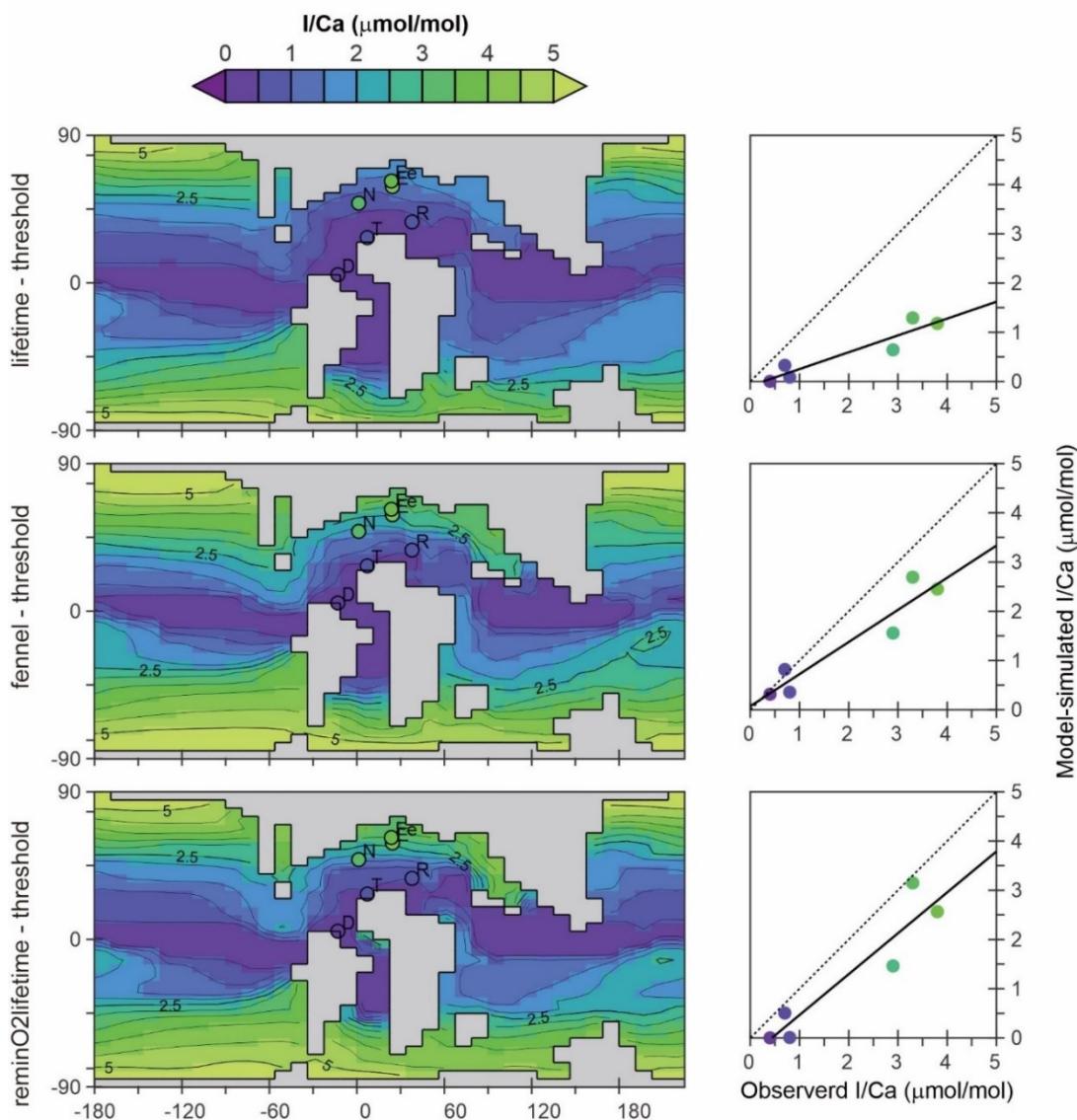
Figure 9. The pre-OAE2 I/Ca field derived from cGENIE [IO₃⁻] simulations, and the comparison between modeled and observed I/Ca from sections.

We first note that both 'lifetime' and 'fennel' iodine oxidation parameterizations in conjunction with a threshold of IO_3^- reduction and internally generated GENIE-[O_2], give rise to identical parameter values (Table 2). We infer that this is because the modern ocean is predominately well-oxygenated and hence there is little inhibition of I^- oxidation in practice. In the Cretaceous environment, although I^- oxidation inhibition should be widespread, the M-scores are similar (Fig. 8). The rate of I^- oxidation in well oxygenated seawater is likely then critical in explaining elevated I/Ca values at higher Cretaceous latitudes. However, simply decreasing the lifetime in the modern ocean would result in an under estimation of surface ocean [I^-]. The 'fennel-threshold' combination under WOA-[O_2] reveals a trade-off that solves this – a decreased I^- lifetime compensated for by increased rates of I^- release to the ocean interior

677   directly through the biological pump and elevated cellular I:C (3.5×10^{-4} mol/mol vs. 1.5×10^{-4} mol/mol). In the

678   Cretaceous ocean this combination allows for both sharper latitudinal gradients in [IO_3^-] (and hence I/Ca) to develop,

679   as well as steeper vertical gradients which allow for non-zero I/Ca values at low latitudes to be captured (cross-plot in

680   Fig. 9). This slight enhancement of the upper ocean [IO_3^-] gradient is also apparent in the present-day analysis (Fig.

681   6). The combination of 'reminO2lifetime' with a reduction threshold works similarly – a shorter lifetime for I$^-$ under

682   oxic conditions offset in the modern ocean by elevated cellular I:C (Table 2). However, in this case, our gridded

683   parameter search identifies the trade-off as producing the highest M-score for both modelled and WOA oxygen

684   distributions.

685   What we learn from this is that the cGENIE iodine cycle tuned to modern observations has predictive power

686   under a very different state of ocean oxygenation (and circulation and operation of biological pump). However, this

687   is not true for every choice of parameterization, and the simple 'lifetime-threshold' combination, which when

688   calibrated was statistically almost the best representation of the iodine cycle, was unable to reproduce the latitudinal

689   I/Ca gradients in the Cretaceous ocean. Shortening the lifetime (and adding an inhibition term) together with increasing

690   the assumed cellular I:C, maintains fidelity in simulating the modern ocean whilst much better capturing Cretaceous

691   I/Ca. That even better representations of Cretaceous I/Ca were possible but at the expense of reproducing modern

692   observations adequately hints that improvements in our mechanistic understanding are needed, although all of the

693   above assumes that the simulation of the Cretaceous redox landscape is plausible.

694   One caveat to our paleo comparison is that because the residence time of iodine in the ocean is only around

695   300 kyr, the dissolved iodine inventory of the Cretaceous ocean could have deviated substantially from the modern

696   seawater value that we assume here (500 nM). One possible explanation for the overall underestimation of I/Ca by

697   cGENIE might then be that the Cretaceous iodine inventory was higher than modern (Zhou et al., 2015; Lu et al.,

698   2018). Even a moderate increase (ca. 20-40%) in the ocean iodine inventory (which we did not test here) would

699   presumably act to increase the slope of the regression lines for the parameterization-combinations 'fennel-threshold'

700   and 'reminO2lifetime-threshold' and bring them close to the 1:1 line (Fig. 9). Another uncertainty concerns the

701   potential impact on carbonate I/Ca ratios of different-from-modern dissolved calcium concentrations in the Cretaceous

702   ocean. The calcite crystal growth experiments of Zhou et al. [2014] on which we base our model-simulated I/Ca values

703   were carried out in synthetic solutions and not seawater. The partition coefficient K_D was calculated as [I/Ca]/[IO_3^-]

704   and as a result our model formulation is independent of the ambient Ca^{2+} concentration. New I/Ca carbonate

705   precipitation experiments that explicitly account for the geological range in seawater composition would help increase

706   confidence in the model-simulated I/Ca values and hence improve the model simulation comparison possible with

707   geological observations.

708

709   **4.4.   Choice of marine iodine cycle representation in cGENIE**

710   The risk in tuning model parameters to fit some data target is always that the processes being tuned are distorted to

711   accommodate an underlying structural error with the model. In this paper we illustrated how sub-regional scale ocean

712   oxygenation features such as the Eastern Tropical North Pacific ODZ (Fig. 7) are poorly represented at the resolution

713   of the cGENIE Earth system model, and how this can lead to deficiencies in the simulation of the marine iodine cycle

714 in these regions. Indeed, we found an improved statistical fit to observed iodine speciation data when we imposed a

715 dissolved oxygen climatology to the model grid rather than use the internally – general model [O$_2$] fields (Table 2).

716 In the case of the 'Fennel' parameterization-combination, we end up with two different sets of parameter values – one

717 associated with the best fit to iodine speciation data under cGENIE projected [O$_2$], and one under WOA imposed [O$_2$].

718 Selecting this particular scheme for paleo applications would appear to create a conundrum – whether (a) to choose

719 the cGENIE [O$_2$] derived parameter value set and accept that model deficiencies were being implicitly corrected for

720 in simulating marine iodine cycling and hence imposing a potential bias on paleo I/Ca, or (b) accept WOA [O$_2$] derived

721 parameter values. The choice would arguably be to accept the less potentially biased parameter value set (b),

722 particularly as the relatively small-scale ODZ features of the modern ocean may be expanded to the regional-to-global

723 scale in deeper time oceans and hence the redox features driving iodate reduction would become much more tractable

724 for a model of the resolution of cGENIE.

725   However, we note that this choice does not exist for parameterization-combinations 'lifetime-threshold' and

726 'reminO2lifetime-threshold'. In both cases the sets of optimal parameter values are the same, whether derived from

727 cGENIE projected [O$_2$] or WOA imposed [O$_2$] (Table 2). This gives us confidence that both these schemes are

728 relatively agnostic to the details of how the modern oxygen cycle is simulated, and that errors in the simulation of sub-

729 regional-scale ocean oxygenation features are not critical. (We note that iodine speciation data is still fitted better

730 under WOA imposed [O$_2$].) The choice of how to best represent the marine iodine cycle in cGENIE is then a choice

731 between 'lifetime-threshold', which has been used in a similar form previously (Lu et al., 2018) and is capable of the

732 best fit to modern observations, or 'reminO2lifetime-threshold'. While 'lifetime-threshold' might be preferable for

733 more recent geological time and ocean ODZs similar to the present-day, it fails to account for I/Ca contrasts under

734 more extreme redox gradients (Fig. 9). Although more difficult to interpret mechanistically, in suppressing the rate of

735 I$^-$ oxidation under low ambient [O$_2$], 'reminO2lifetime-threshold' appears to be the more appropriate paleo choice.

736   We note that to achieve improved simulation of sub-regional scale features of the ocean redox landscape,

737 future paleo cGENIE model I/Ca applications could make use of the coupled GENIE-PLASIM climate configuration

738 (Holden et al., 2016) . In this, the ocean circulation model is implemented on a higher resolution grid (64 × 32 with

739 32 vertical levels) and includes a coupled atmospheric GCM component (hence enabling interannual variability). It is

740 also capable of being configured with different continental configurations for paleo climate questions (e.g. Keery et

741 al., 2018).

742

5. Conclusions

Using the cGENIE Earth system model, we performed a series of ensemble experiments to determine suitable parameterizations to represent the marine iodine cycle and identified the best performing combinations of parameter values in each case. We found that the optimized parameter values associated with, water column IO_3^- reduction and I^- oxidation, plus IO_3^- planktonic uptake (and subsequence I^- release during remineralization), all fell within the range of field and experiment observations and hence could be considered plausible. Three iodine cycling parameterization -combinations, 'lifetime-threshold', 'reminO2lifetime-threshold', and 'fennel-threshold' were considered as viable candidates following our tests of the global ocean model M-score, and model-data comparisons made across specific iodine gradients (euphotic latitudinal distribution, depth distribution, and ODZ distribution). We further evaluated the plausibility of our parameterizations and their paleo and ocean deoxygenation applicability by contrasting forward-proxy model generated I/Ca values against observations, taking the (pre-OAE2) Cretaceous redox landscape as a case study. While we highlighted the importance of improving the simulation of dissolved oxygen distributions in models, we also found that our conclusions regarding preferred parameterizations and even specific parameter values was not overly dependent on the specific details of the simulated modern ODZs. Overall, while some model-data discrepancies emerge for both modern and paleo, these highlight that future observational and/or experimental work is necessary to better constrain modern iodine cycling mechanisms and related spatiotemporal heterogeneities but that representations of the marine iodine cycle in an Earth system model based on modern observations and mechanistic knowledge appear transferrable to interpreting the geological record of the I/Ca oxygenation proxy.

Code availability. The code for the version of the 'muffin' release of the cGENIE Earth system model used in this paper, is tagged as v0.9.54, and is assigned a DOI: 10.5281/zenodo.13376310. Configuration files for the specific experiments presented in the paper can be found in the directory: genie-userconfigs/PUBS/published/Cheng_et_al.Biogeosciences.2024. Details of the experiments, plus the command line needed to run each one, are given in the readme.txt file in that directory. All other configuration files and boundary conditions are provided as part of the code release. A manual detailing code installation, basic model configuration, tutorials covering various aspects of model configuration, experimental design, and output, plus the processing of results, is assigned a DOI: 10.5281/zenodo.1407657.

References

Amachi, S., Kawaguchi, N., Muramatsu, Y., Tsuchiya, S., Watanabe, Y., Shinoyama, H., and Fujii, T.: Dissimilatory iodate reduction by marine Pseudomonas sp. strain SCT, Appl. Environ. Microbiol., 73, 5725–5730, https://doi.org/10.1128/AEM.00241-07, 2007.

Boscolo-Galazzo, F., Crichton, K. A., Ridgwell, A., Mawbey, E. M., Wade, B. S., and Pearson, P. N.: Temperature controls carbon cycling and biological evolution in the ocean twilight zone, Science (80-.)., 371, 1148–1152, https://doi.org/10.1126/science.abb6643, 2021.

Bowman, C. N., Lindskog, A., Kozik, N. P., Richbourg, C. G., Owens, J. D., and Young, S. A.: Integrated sedimentary, biotic, and paleoredox dynamics from multiple localities in southern Laurentia during the late Silurian (Ludfordian) extinction event, Palaeogeogr. Palaeoclimatol. Palaeoecol., 553, 109799, https://doi.org/10.1016/j.palaeo.2020.109799, 2020.

Broecker, W. S. and Peng, T. H.: Tracers in the Sea., https://doi.org/10.1016/0016-7037(83)90075-3, 1983.

Campos, M. L. A. M., Farrenkopf, A. M., Jickells, T. D., and Luther, G. W.: A comparison of dissolved iodine

797   cycling at the Bermuda Atlantic Time-series station and Hawaii Ocean Time-series station, Deep. Res. Part II Top.

798   Stud. Oceanogr., 43, 455–466, https://doi.org/10.1016/0967-0645(95)00100-x, 1996.

799   Chance, R., Weston, K., Baker, A. R., Hughes, C., Malin, G., Carpenter, L., Meredith, M. P., Clarke, A., Jickells, T.

800   D., Mann, P., and Rossetti, H.: Seasonal and interannual variation of dissolved iodine speciation at a coastal

801   Antarctic site, Mar. Chem., 118, 171–181, https://doi.org/10.1016/j.marchem.2009.11.009, 2010.

802   Chance, R., Baker, A. R., Carpenter, L., and Jickells, T. D.: The distribution of iodide at the sea surface, Environ.

803   Sci. Process. Impacts, 16, 1841–1859, https://doi.org/10.1039/c4em00139g, 2014.

804   Chance, R., Tinel, L., Sherwen, T., Baker, A., Bell, T., Brindle, J., Campos, M., Croot, P., Ducklow, H., He, P.,

805   Hoogakker, B., Hopkins, F., Hughes, C., Jickells, T., Loades, D., Reyes Macaya, D., Mahajan, A., Malin, G.,

806   Phillips, D., Sinha, A., Sarkar, A., Roberts, I., Roy, R., Song, X., Winklebauer, H., Wuttig, K., Yang, M., Zhou, P.,

807   and Carpenter, L.: Global sea-surface iodide observations, 1967-2018., https://doi.org/doi:10.5285/7e77d6b9-83fb-

808   41e0-e053-6c86abc069d0, 2019.

809   Chapman, P.: Changes in iodine speciation in the Benguela current upwelling system, Deep Sea Res. Part A,

810   Oceanogr. Res. Pap., 30, 1247–1259, https://doi.org/10.1016/0198-0149(83)90083-3, 1983.

811   Councell, T. B., Landa, E. R., and Lovley, D. R.: Microbial reduction of iodate, Water. Air. Soil Pollut., 100, 99–

812   106, 1997.

813   Crichton, K. A., Wilson, J. D., Ridgwell, A., and Pearson, P. N. P. N.: Calibration of temperature-dependent ocean

814   microbial processes in the cGENIE.muffin (v0.9.13) Earth system model, Geosci. Model Dev., 14, 125–149,

815   https://doi.org/10.5194/gmd-14-125-2021, 2021.

816   Cutter, G. A., Moffett, J. G., Nielsdóttir, M. C., and Sanial, V.: Multiple oxidation state trace elements in suboxic

817   waters off Peru: In situ redox processes and advective/diffusive horizontal transport, Mar. Chem., 201, 77–89,

818   https://doi.org/10.1016/j.marchem.2018.01.003, 2018.

819   Dalsgaard, T., Stewart, F. J., Thamdrup, B., De Brabandere, L., Revsbech, N. P., Ulloa, O., Canfield, D. E., and

820   Delong, E. F.: Oxygen at nanomolar levels reversibly suppresses process rates and gene expression in anammox and

821   denitrification in the oxygen minimum zone off Northern Chile, MBio, 5, 1–14,

822   https://doi.org/10.1128/mBio.01966-14, 2014.

823   Ding, Y., Sun, W., Liu, S., Xie, J., Tang, D., Zhou, X., Zhou, L., Li, Z., Song, J., Li, Z., Xu, H., Tang, P., Liu, K.,

824   Li, W., and Chen, D.: Low oxygen levels with high redox heterogeneity in the late Ediacaran shallow ocean:

825   Constraints from I/(Ca + Mg) and Ce/Ce* of the Dengying Formation, South China, Geobiology, 20, 790–809,

826   https://doi.org/10.1111/gbi.12520, 2022.

827   Edwards, A. and Truesdale, V. W.: Regeneration of inorganic iodine species in loch etive, a natural leaky incubator,

828   Estuar. Coast. Shelf Sci., 45, 357–366, https://doi.org/10.1006/ecss.1996.0185, 1997.

829   Edwards, C. T., Fike, D. A., Saltzman, M. R., Lu, W., and Lu, Z.: Evidence for local and global redox conditions at

830   an Early Ordovician (Tremadocian) mass extinction, Earth Planet. Sci. Lett., 481, 125–135,

831   https://doi.org/10.1016/j.epsl.2017.10.002, 2018.

832   Edwards, N. R. and Marsh, R.: Uncertainties due to transport-parameter sensitivity in an efficient 3-D ocean-climate

833   model, Clim. Dyn., 415–433, https://doi.org/10.1007/s00382-004-0508-8, 2005.

834   Elderfield, H. and Truesdale, V. W.: On the biophilic nature of iodine in seawater, Earth Planet. Sci. Lett., 50, 105–

835   114, https://doi.org/10.1016/0012-821X(80)90122-3, 1980.

836   Fang, H., Tang, D., Shi, X., Zhou, L., Zhou, X., Wu, M., Song, H., and Riding, R.: Early Mesoproterozoic Ca-

837   carbonate precipitates record fluctuations in shallow marine oxygenation, Precambrian Res., 373, 106630,

838   https://doi.org/10.1016/j.precamres.2022.106630, 2022.

839   Farrenkopf, A. M. and Luther, G. W.: Iodine chemistry reflects productivity and denitrification in the Arabian Sea:

840   Evidence for flux of dissolved species from sediments of western India into the OMZ, Deep. Res. Part II Top. Stud.

841   Oceanogr., 49, 2303–2318, https://doi.org/10.1016/S0967-0645(02)00038-3, 2002.

842   Farrenkopf, A. M., Dollhopf, M. E., Chadhain, S. N., Luther, G. W., and Nealson, K. H.: Reduction of iodate in

843   seawater during Arabian Sea shipboard incubations and in laboratory cultures of the marine bacterium Shewanella

844   putrefaciens strain MR-4, Mar. Chem., 57, 347–354, https://doi.org/10.1016/S0304-4203(97)00039-X, 1997.

845   Fennel, K., Follows, M., and Falkowski, P. G.: The co-evolution of the nitrogen, carbon and oxygen cycles in the

846   Proterozoic ocean, Am. J. Sci., 305, 526–545, 2005.

847   Garcia, H. E., Weathers, K., Paver, C. R., Smolyar, I., Boyer, T. P., Locarnini, R. A., Zweng, M. M., Mishonov, A.

848   V., Baranova, O. K., Seidov, D., and Reagan, J. R.: Volume 3: Dissolved Oxygen, Apparent Oxygen Utilization, and

849   Oxygen Saturation. A. Mishonov Technical Ed.; NOAA Atlas NESDIS 83, World Ocean Atlas 2018, 38 pp., 2018.

850   Hardisty, D. S., Lu, Z., Planavsky, N. J., Bekker, A., Philippot, P., Zhou, X., and Lyons, T. W.: An iodine record of

851   Paleoproterozoic surface ocean oxygenation, Geology, 42, 619–622, https://doi.org/10.1130/G35439.1, 2014.

852   Hardisty, D. S., Lu, Z., Bekker, A., Diamond, C. W., Gill, B. C., Jiang, G., Kah, L. C., Knoll, A. H., Loyd, S. J.,

853   Osburn, M. R., Planavsky, N. J., Wang, C., Zhou, X., and Lyons, T. W.: Perspectives on Proterozoic surface ocean

854   redox from iodine contents in ancient and recent carbonate, Earth Planet. Sci. Lett., 463, 159–170,

855   https://doi.org/10.1016/j.epsl.2017.01.032, 2017.

856   Hardisty, D. S., Horner, T. J., Wankel, S. D., Blusztajn, J., and Nielsen, S. G.: Experimental observations of marine

857   iodide oxidation using a novel sparge-interface MC-ICP-MS technique, Chem. Geol., 532, 119360,

858   https://doi.org/10.1016/j.chemgeo.2019.119360, 2020.

859   Hardisty, D. S., Horner, T. J., Evans, N., Moriyasu, R., Babbin, A. R., Wankel, S. D., Moffett, J. W., and Nielsen, S.

860   G.: Limited iodate reduction in shipboard seawater incubations from the Eastern Tropical North Pacific oxygen

861   deficient zone, Earth Planet. Sci. Lett., 554, 116676, https://doi.org/10.1016/j.epsl.2020.116676, 2021.

862   Hashim, M. S., Burke, J. E., Hardisty, D. S., and Kaczmarek, S. E.: Iodine incorporation into dolomite:

863   Experimental constraints and implications for the iodine redox proxy and Proterozoic Ocean, Geochim. Cosmochim.

864   Acta, 338, 365–381, https://doi.org/10.1016/j.gca.2022.10.027, 2022.

865   He, P., Hou, X., and Aldahan, A.: Iodine isotopes species fingerprinting environmental conditions in surface water

866   along the northeastern Atlantic Ocean, Sci. Rep., 3, 1–9, https://doi.org/10.1038/srep02685, 2013.

867   Hepach, H., Hughes, C., Hogg, K., Collings, S., and Chance, R.: Senescence as the main driver of iodide release

868   from a diverse range of marine phytoplankton, Biogeosciences, 17, 2453–2471, https://doi.org/10.5194/bg-17-2453-

869   2020, 2020.

870   Holden, P. B., Edwards, N. R., Fraedrich, K., Kirk, E., Lunkeit, F., and Zhu, X.: PLASIM-GENIE v1.0: A new

871   intermediate complexity AOGCM, Geosci. Model Dev., 9, 3347–3361, https://doi.org/10.5194/gmd-9-3347-2016,

872   2016.

873   Hughes, C., Barton, E., Hepach, H., Chance, R., Wadley, M. R., Pickering, M. D., Hogg, K., Pommerening-r, A.,

874   Stevens, D. P., and Jickells, T. D.: Oxidation of iodide to iodate by cultures of marine ammonia-oxidising bacteria,

875   Mar. Chem., 234, https://doi.org/10.1016/j.marchem.2021.104000, 2021.

876   Hülse, D., Arndt, S., and Ridgwell, A.: Mitigation of Extreme Ocean Anoxic Event Conditions by Organic Matter

877   Sulfurization, Paleoceanogr. Paleoclimatology, 34, 476–489, https://doi.org/10.1029/2018PA003470, 2019.

878   Jia-zhong, Z. and Whitfield, M.: KINETICS OF INORGANIC REDOX REACTIONS IN SEAWATER I . The

879   reduction of iodate by bisulphide Micro-organisms play a dominant role in the diagenesis of organic-rich sediments .

880   The oxidative breakdown of the organic matter , with the accom- panying reductio, Science (80-.)., 19, 121–137,

881   1986.

882   Jiang, Z., Cui, M., Qian, L., Jiang, Y., Shi, L., Dong, Y., Li, J., and Wang, Y.: Abiotic and Biotic Reduction of

883   Iodate Driven by Shewanella oneidensis MR-1 , Environ. Sci. Technol., https://doi.org/10.1021/acs.est.3c06490,

884   2023.

885   Keery, J. S., Holden, P. B., and Edwards, N. R.: Sensitivity of the Eocene climate to CO2 and orbital variability,

886   Clim. Past, 14, 215–238, https://doi.org/10.5194/cp-14-215-2018, 2018.

887   Kerisit, S. N., Smith, F. N., Saslow, S. A., Hoover, M. E., Lawter, A. R., and Qafoku, N. P.: Incorporation Modes of

888   Iodate in Calcite, Environ. Sci. Technol., 52, 5902–5910, https://doi.org/10.1021/acs.est.8b00339, 2018.

889   Laws, E. A., Falkowski, P. G., Smith, W. O., Ducklow, H., and James J McCarthy: Temperature effects on export

890   production in the open ocean, Global Biogeochem. Cycles, 14, 1231–1246, 2000.

891   Liu, A., Tang, D., Shi, X., Zhou, X., Zhou, L., Shang, M., Li, Y., and Fang, H.: Mesoproterozoic oxygenated deep

892   seawater recorded by early diagenetic carbonate concretions from the Member IV of the Xiamaling Formation,

893   North China, Precambrian Res., 341, 105667, https://doi.org/10.1016/j.precamres.2020.105667, 2020.

894   Lu, W., Ridgwell, A., Thomas, E., Hardisty, D. S., Luo, G., Algeo, T. J., Saltzman, M. R., Gill, B. C., Shen, Y.,

895   Ling, H. F., Edwards, C. T., Whalen, M. T., Zhou, X., Gutchess, K. M., Jin, L., Rickaby, R. E. M., Jenkyns, H. C.,

896   Lyons, T. W., Lenton, T. M., Kump, L. R., and Lu, Z.: Late inception of a resiliently oxygenated upper ocean,

897   Science (80-.)., 361, 174–177, https://doi.org/10.1126/science.aar5372, 2018.

898   Lu, W., Rickaby, R. E. M., Hoogakker, B. A. A., Rathburn, A. E., Burkett, A. M., Dickson, A. J., Martínez-Méndez,

899   G., Hillenbrand, C. D., Zhou, X., Thomas, E., and Lu, Z.: I/Ca in epifaunal benthic foraminifera: A semi-

900   quantitative proxy for bottom water oxygen in a multi-proxy compilation for glacial ocean deoxygenation, Earth

901   Planet. Sci. Lett., 533, https://doi.org/10.1016/j.epsl.2019.116055, 2020a.

902   Lu, W., Dickson, A. J., Thomas, E., Rickaby, R. E. M., Chapman, P., and Lu, Z.: Refining the planktic foraminiferal

903   I/Ca proxy: Results from the Southeast Atlantic Ocean, Geochim. Cosmochim. Acta, 287, 318–327,

904   https://doi.org/10.1016/j.gca.2019.10.025, 2020b.

905   Lu, Z., Jenkyns, H. C., and Rickaby, R. E. M.: Iodine to calcium ratios in marine carbonate as a paleo-redox proxy

906   during oceanic anoxic events, Geology, 38, 1107–1110, https://doi.org/10.1130/G31145.1, 2010.

907   Lu, Z., Hoogakker, B. A. A., Hillenbrand, C.-D., Zhou, X., Thomas, E., Gutchess, K. M., Lu, W., Jones, L., and

Rickaby, R. E. M.: Oxygen depletion recorded in upper waters of the glacial Southern Ocean, Nat. Commun., 7, 1–8, https://doi.org/10.1038/ncomms11146, 2016.

Luther, G. W.: Review on the physical chemistry of iodine transformations in the oceans, Front. Mar. Sci., 10, 1–16, https://doi.org/10.3389/fmars.2023.1085618, 2023.

Luther, G. W. and Campbell, T.: Iodine speciation in the water column of the Black Sea, Deep Sea Res. Part A. Oceanogr. Res. Pap., 38, S875–S882, https://doi.org/10.1016/s0198-0149(10)80014-7, 1991.

Luther, G. W., Wu, J., and Cullen, J. B.: Redox Chemistry of Iodine in Seawater, Adv. Chem., 135–155, 1995.

Luther, W.: Iodine Chemistry in the Water the Chesapeake Bay : Evidence Iodine Forms Column of for Organic, Esruarine, Coast. Shelf Sci., 32, 267–279, 1991.

Marsh, R., Müller, S. A., Yool, A., and Edwards, N. R.: Incorporation of the C-GOLDSTEIN efficient climate model into the GENIE framework: "eb_go_gs" configurations of GENIE, Geosci. Model Dev., 4, 957–992, https://doi.org/10.5194/gmd-4-957-2011, 2011.

Martin, T. S., Primeau, F., and Casciotti, K. L.: Modeling oceanic nitrate and nitrite concentrations and isotopes using a 3-D inverse N cycle model, Biogeosciences, 347–367, 2019.

Matsumoto, K.: Radiocarbon-based circulation age of the world oceans, J. Geophys. Res. Ocean., 112, 1–7, https://doi.org/10.1029/2007JC004095, 2007.

Monteiro, F. M., Pancost, R. D., Ridgwell, A., and Donnadieu, Y.: Nutrients as the dominant control on the spread of anoxia and euxinia across the Cenomanian-Turonian oceanic anoxic event (OAE2): Model-data comparison, Paleoceanography, 27, https://doi.org/10.1029/2012PA002351, 2012.

Moriyasu, R., Evans, N., Bolster, K. M., Hardisty, D. S., and Moffett, J. W.: The Distribution and Redox Speciation of Iodine in the Eastern Tropical North Pacific Ocean, Global Biogeochem. Cycles, 34, 1–23, https://doi.org/10.1029/2019GB006302, 2020.

Moriyasu, R., Bolster, K. M., Hardisty, D. S., Kadko, D. C., Stephens, M. P., and Moffett, J. W.: Meridional survey of the Central Pacific reveals iodide accumulation in equatorial surface waters and benthic sources in the abyssal plain, Global Biogeochem. Cycles, https://doi.org/10.1029/2021GB007300, 2023.

Panchuk, K., Ridgwell, A., and Kump, L. R.: Sedimentary response to Paleocene-Eocene thermal maximum carbon release: A model-data comparison, Geology, 36, 315–318, https://doi.org/10.1130/G24474A.1, 2008.

Podder, J., Lin, J., Sun, W., Botis, S. M., Tse, J., Chen, N., Hu, Y., Li, D., Seaman, J., and Pan, Y.: Iodate in calcite and vaterite: Insights from synchrotron X-ray absorption spectroscopy and first-principles calculations, Geochim. Cosmochim. Acta, 198, 218–228, https://doi.org/10.1016/j.gca.2016.11.032, 2017.

Pohl, A., Lu, Z., Lu, W., Stockey, R. G., Elrick, M., Li, M., Desrochers, A., Shen, Y., He, R., Finnegan, S., and Ridgwell, A.: Vertical decoupling in Late Ordovician anoxia due to reorganization of ocean circulation, Nat. Geosci., 14, 868–873, https://doi.org/10.1038/s41561-021-00843-9, 2021.

Pohl, A., Ridgwell, A., Stockey, R. G., Thomazo, C., Keane, A., Vennin, E., and Scotese, C. R.: Continental configuration controls ocean oxygenation during the Phanerozoic, Nature, 608, 523–527, https://doi.org/10.1038/s41586-022-05018-z, 2022.

Rapp, I., Schlosser, C., Barraqueta, J. M., Wenzel, B., Lüdke, J., and Scholten, J.: Controls on redox-sensitive trace

945   metals in the Mauritanian oxygen minimum zone, 4157–4182, 2019.

946   Rapp, I., Schlosser, C., Browning, T. J., Wolf, F., Le Moigne, F. A. C., Gledhill, M., and Achterberg, E. P.: El Niño-

947   Driven Oxygenation Impacts Peruvian Shelf Iron Supply to the South Pacific Ocean, Geophys. Res. Lett., 47,

948   https://doi.org/10.1029/2019GL086631, 2020.

949   Reinhard, C. T. and Planavsky, N. J.: The History of Ocean Oxygenation, Ann. Rev. Mar. Sci., 14, 331–353,

950   https://doi.org/10.1146/annurev-marine-031721-104005, 2022.

951   Reinhard, C. T., Planavsky, N. J., Olson, S. L., Lyons, T. W., and Erwin, D. H.: Earth's oxygen cycle and the

952   evolution of animal life, Proc. Natl. Acad. Sci. U. S. A., 113, 8933–8938, https://doi.org/10.1073/pnas.1521544113,

953   2016.

954   Reinhard, C. T., Olson, S. L., Turner, S. K., Pälike, C., Kanzaki, Y., and Ridgwell, A.: Oceanic and atmospheric

955   methane cycling in the cGENIE Earth system model, Geosci. Model Dev., 1–45, https://doi.org/10.5194/gmd-2020-

956   32, 2020.

957   Remmelzwaal, S. R. C., Dixon, S., Parkinson, I. J., Schmidt, D. N., Monteiro, F. M., Sexton, P., Fehr, M. A.,

958   Peacock, C., Donnadieu, Y., and James, R. H.: Investigating Ocean Deoxygenation During the PETM Through the

959   Cr Isotopic Signature of Foraminifera, Paleoceanogr. Paleoclimatology, 34, 917–929,

960   https://doi.org/10.1029/2018PA003372, 2019.

961   Reyes-Umana, V., Henning, Z., Lee, K., Barnum, T. P., and Coates, J. D.: Genetic and phylogenetic analysis of

962   dissimilatory iodate-reducing bacteria identifies potential niches across the world's oceans, ISME J.,

963   https://doi.org/10.1038/s41396-021-01034-5, 2021.

964   Ridgwell, A., Hargreaves, J. C., Edwards, N. R., Annan, J. D., Lenton, T. M., Marsh, R., Yool, A., and Watson, A.:

965   Marine geochemical data assimilation in an efficient Earth system model of global biogeochemical cycling,

966   Biogeosciences, 4, 87–104, https://doi.org/10.5194/bg-4-87-2007, 2007.

967   Rue, E. L., Smith, G. J., Cutter, G. A., and Bruland, K. W.: The response of trace element redox couples to suboxic

968   conditions in the water column, Deep. Res. Part I Oceanogr. Res. Pap., 44, 113–134, https://doi.org/10.1016/S0967-

969   0637(96)00088-X, 1997.

970   Schnur, A. A., Sutherland, K. M., Hansel, C. M., and Hardisty, D. S.: Rates and pathways of iodine speciation

971   transformations at the Bermuda Atlantic Time Series, Front. Mar. Sci., 1–14,

972   https://doi.org/10.3389/fmars.2023.1272870, 2024.

973   Scholz, F., Hardisty, D. S., and Dale, A. W.: Early Diagenetic Controls on Sedimentary Iodine Release and Iodine-

974   To-Organic Carbon Ratios in the Paleo-Record, Global Biogeochem. Cycles, 38,

975   https://doi.org/10.1029/2023GB007919, 2024.

976   Shang, M., Tang, D., Shi, X., Zhou, L., Zhou, X., Song, H., and Jiang, G.: A pulse of oxygen increase in the early

977   Mesoproterozoic ocean at ca. 1.57–1.56 Ga, Earth Planet. Sci. Lett., 527, 115797,

978   https://doi.org/10.1016/j.epsl.2019.115797, 2019.

979   Ştreangă, I.-M., Repeta, D. J., Blusztajn, J. S., and Horner, T. J.: Speciation and cycling of iodine in the subtropical

980   North Paci fi c Ocean, Front. Mar. Sci., 1–15, https://doi.org/10.3389/fmars.2023.1272968, 2024.

981   Tang, D., Fang, H., Shi, X., Liang, L., Zhou, L., Xie, B., Huang, K., Zhou, X., Wu, M., and Riding, R.:

982 Mesoproterozoic Molar Tooth Structure Related to Increased Marine Oxygenation, J. Geophys. Res.

983 Biogeosciences, 128, 1–18, https://doi.org/10.1029/2022jg007077, 2023.

984 Thamdrup, B., Dalsgaard, T., and Revsbech, N. P.: Widespread functional anoxia in the oxygen minimum zone of

985 the Eastern South Pacific, Deep. Res. Part I Oceanogr. Res. Pap., 65, 36–45,

986 https://doi.org/10.1016/j.dsr.2012.03.001, 2012.

987 Truesdale, V. W., Bale, A. J., and Woodward, E. M. S.: The meridional distribution of dissolved iodine in near-

988 surface waters of the Atlantic Ocean, Prog. Oceanogr., 45, 387–400, https://doi.org/10.1016/S0079-6611(00)00009-

989 4, 2000.

990 Truesdale, V. W., Watts, S. F., and Rendell, A. R.: On the possibility of iodide oxidation in the near-surface of the

991 Black Sea and its implications to iodine in the general ocean, Deep. Res. Part I, 48, 2397–2412, 2001.

992 Truesdale, V. W., Nausch, G., and Waite, T. J.: The effects of the 2001 Barotropic intrusion of bottom-water upon

993 the vertical distribution of inorganic iodine in the Gotland Deep, Cont. Shelf Res., 55, 155–167,

994 https://doi.org/10.1016/j.csr.2013.01.005, 2013.

995 Tsunogai, S.: Iodine in the deep water of the ocean, Deep. Res., 18, 913–919, 1971.

996 Uahengo, C. I., Shi, X., Jiang, G., and Vatuva, A.: Transient shallow-ocean oxidation associated with the late

997 Ediacaran Nama skeletal fauna: Evidence from iodine contents of the Lower Nama Group, southern Namibia,

998 Precambrian Res., 343, 105732, https://doi.org/10.1016/j.precamres.2020.105732, 2020.

999 Wadley, M. R., Stevens, D. P., Jickells, T. D., Hughes, C., Chance, R., Hepach, H., Tinel, L., and Carpenter, L. J.: A

1000 Global Model for Iodine Speciation in the Upper Ocean, Global Biogeochem. Cycles, 34, 0–3,

1001 https://doi.org/10.1029/2019GB006467, 2020.

1002 Watterson, I. G.: Non-dimensional measures of climate model performance, Int. J. Climatol., 16, 379–391,

1003 https://doi.org/10.1002/(SICI)1097-0088(199604)16:4<379::AID-JOC18>3.0.CO;2-U, 1996.

1004 Wei, B., Tang, D., Shi, X., Lechte, M., Zhou, L., Zhou, X., and Song, H.: A Pulsed Oxygenation in Terminal

1005 Paleoproterozoic Ocean: Evidence From the Transition Between the Chuanlinggou and Tuanshanzi Formations,

1006 North China, Geochemistry, Geophys. Geosystems, 22, 1–23, https://doi.org/10.1029/2020GC009612, 2021.

1007 Wong, G. T. F. and Brewer, P. G.: The marine chemistry of iodine in anoxic basins, Geochim. Cosmochim. Acta,

1008 41, 151–159, https://doi.org/10.1016/0016-7037(77)90195-8, 1977.

1009 Wong, G. T. F., Takayanagi, K., and Todd, J. F.: Dissolved iodine in waters overlying and in the Orca Basin, Gulf of

1010 Mexico, Mar. Chem., 17, 177–183, https://doi.org/10.1016/0304-4203(85)90072-6, 1985.

1011 Wong, G. T. F., Piumsomboon, A. U., Dunstan, W. M., Wong, G. T. F., Piumsomboon, A. U., and Dunstan, W. M.:

1012 The transformation of iodate to iodide in marine phytoplankton cultures, Mar. Geol. Prog. Ser., 237, 27–39, 2002.

1013 Yamazaki, C., Kashiwa, S., Horiuchi, A., and Kasahara, Y.: A novel dimethylsulfoxide reductase family of

1014 molybdenum enzyme , Idr , is involved in iodate respiration by Pseudomonas sp . SCT, 22, 2196–2212,

1015 https://doi.org/10.1111/1462-2920.14988, 2020.

1016 Yu, Y., Chen, Y., Li, D., and Su, J.: A transient oxygen increase in the Mesoproterozoic ocean at ~1.44 Ga:

1017 Geochemical evidence from the Tieling Formation, North China Platform, Precambrian Res., 369, 106527,

1018 https://doi.org/10.1016/j.precamres.2021.106527, 2022.

1019   Zhang, S., Xu, C., Creeley, D., Ho, Y. F., Li, H. P., Grandbois, R., Schwehr, K. A., Kaplan, D. I., Yeager, C. M.,

1020   Wellman, D., and Santschi, P. H.: Response to comment on "iodine-129 and iodine-127 speciation in groundwater at

1021   hanford site, U.S.: Iodate incorporation into calcite," Environ. Sci. Technol., 47, 13205–13206,

1022   https://doi.org/10.1021/es4046132, 2013.

1023   Zhou, X., Thomas, E., Rickaby, R. E. M., Winguth, A. M. E., and Lu, Z.: I/Ca evidence for upper ocean

1024   deoxygenation during the PETM, Paleoceanography, 29, 964–975, https://doi.org/10.1002/2014PA002702, 2014.

1025   Zhou, X., Jenkyns, H. C., Owens, J. D., Junium, C. K., Zheng, X. Y., Sageman, B. B., Hardisty, D. S., Lyons, T. W.,

1026   Ridgwell, A., and Lu, Z.: Upper ocean oxygenation dynamics from I/Ca ratios during the Cenomanian-Turonian

1027   OAE 2, Paleoceanography, 30, 510–526, https://doi.org/10.1002/2014PA002741, 2015.

1028   Žic, V., Carić, M., and Ciglenečki, I.: The impact of natural water column mixing on iodine and nutrient speciation

1029   in a eutrophic anchialine pond (Rogoznica Lake, Croatia), Estuar. Coast. Shelf Sci., 133, 260–272,

1030   https://doi.org/10.1016/j.ecss.2013.09.008, 2013.

1031